



CHORUS

This is the accepted manuscript made available via CHORUS. The article has been published as:

Redshift-space distortions in massive neutrino and evolving dark energy cosmologies

Amol Upadhye, Juliana Kwan, Adrian Pope, Katrin Heitmann, Salman Habib, Hal Finkel, and Nicholas Frontiere

Phys. Rev. D **93**, 063515 — Published 16 March 2016

DOI: [10.1103/PhysRevD.93.063515](https://doi.org/10.1103/PhysRevD.93.063515)

Redshift-space distortions in massive neutrino and evolving dark energy cosmologies

Amol Upadhye,¹ Juliana Kwan,² Adrian Pope,³ Katrin Heitmann,^{3,4,5}
Salman Habib,^{3,4,5} Hal Finkel,⁶ and Nicholas Frontiere^{3,7}

¹*Department of Physics, University of Wisconsin–Madison, 1150 University Avenue, Madison, WI 53706*

²*Department of Physics and Astronomy, University of Pennsylvania, Philadelphia, PA 19104*

³*High Energy Physics Division, Argonne National Laboratory, 9700 S. Cass Ave., Lemont, IL 60439*

⁴*Kavli Institute for Cosmological Physics, The University of Chicago, Chicago, IL 60637*

⁵*Mathematics and Computer Science Division, Argonne National Laboratory, 9700 S. Cass Ave., Lemont IL 60439*

⁶*ALCF, Argonne National Laboratory, 9700 S. Cass Ave., Lemont, IL 60439*

⁷*Department of Physics, The University of Chicago, Chicago, IL 60637*

(Dated: February 16, 2016)

Large-scale structure surveys in the coming years will measure the redshift-space power spectrum to unprecedented accuracy, allowing for powerful new tests of the Λ CDM picture as well as measurements of particle physics parameters such as the neutrino masses. We extend the Time-RG perturbative framework to redshift space, computing the power spectrum $P_s(k, \mu)$ in massive neutrino cosmologies with time-dependent dark energy equations of state $w(z)$. Time-RG is uniquely capable of incorporating scale-dependent growth into the $P_s(k, \mu)$ computation, which is important for massive neutrinos as well as modified gravity models. Although changes to $w(z)$ and the neutrino mass fraction both affect the late-time scale-dependence of the non-linear power spectrum, we find that the two effects depend differently on the line-of-sight angle μ . Finally, we use the HACC N-body code to quantify errors in the perturbative calculations. For a Λ CDM model at redshift $z = 1$, our procedure predicts the monopole (quadrupole) to 1% accuracy up to a wave number $0.19h/\text{Mpc}$ ($0.28h/\text{Mpc}$), compared to $0.08h/\text{Mpc}$ ($0.07h/\text{Mpc}$) for the Kaiser approximation and $0.19h/\text{Mpc}$ ($0.16h/\text{Mpc}$) for the current state-of-the-art perturbation scheme. Our calculation agrees with the simulated redshift-space power spectrum even for neutrino masses above the current bound, and for rapidly-evolving dark energy equations of state, $|dw/dz| \sim 1$. Along with this article, we make our redshift-space Time-RG implementation publicly available as the code `redTime`.

I. INTRODUCTION

Two major challenges for cosmology over the next decade are measuring the neutrino masses and constraining the evolution of the dark energy density. The sum of the neutrino masses, a fundamental Standard Model parameter, is bounded from above by cosmological probes [1, 2]: $\sum m_\nu < 0.23$ eV. Improved measurements of large-scale structure and the cosmic microwave background over the next several years will replace this bound with a measurement, possibly allowing us to distinguish between normal and inverted neutrino mass hierarchies [3–9].

Meanwhile, searches for dark energy evolution are entering a decisive era. The cosmological constant Λ , the simplest model of dark energy, is completely consistent with current data [1, 2, 10–17]. However, a cosmological energy density which is 120 orders of magnitude below fundamental scales, yet coincidentally nearly equal to the dark matter density today, requires a great deal of fine-tuning [18–22]. If we consider models in which the dark energy density ρ_{DE} and its equation of state $w_{\text{DE}}(z) = P_{\text{DE}}/\rho_{\text{DE}}$ may vary with redshift z , the uncertainty in dw_{DE}/dz is of order unity today [23]. Current constraints allow “early dark energy” models in which $\rho_{\text{DE}}(z)$ rises rapidly with z , substantially alleviating the tuning and coincidence problems associated with the cosmological constant [24–32]. Over the next ten to fifteen years, constraints on dw_{DE}/dz will improve sub-

stantially, allowing models with $|dw_{\text{DE}}/dz| \sim 1$ to be distinguished decisively from slowly-evolving equations of state [3]. Thus cosmology is poised to answer two fundamental questions about the nature of the universe.

Such powerful cosmological constraints will be made possible by combining probes of the expansion rate $H(z)$, including Type Ia supernova [33] and baryon acoustic oscillation (BAO) [2] surveys, with measurements of the growth factor $D(z)$, including redshift-space distortions (RSD) [34, 35] and weak lensing [36]. Here we are particularly interested in the RSD, which probe the logarithmic growth rate $f(z) = -d \log(D)/d \log(1+z)$. These are measured at quasi-linear scales $10 \text{ Mpc} - 100 \text{ Mpc}$, and they are minimally affected by astrophysical systematics such as baryonic feedback. As a result, perturbative treatments of the redshift-space power spectrum are feasible [37–40].

Time-RG perturbation theory, which directly integrates a system of non-linear equations for the matter power spectrum $P(k)$ (the Fourier transform of the two-point correlation function), was designed for models with scale-dependent growth factors, such as massive neutrino, modified gravity, and clustering dark energy models [41–43]. It is implemented in publicly-available codes including `Copter` [44] and `CLASS` [45]. Its approach to computing the power spectrum is to truncate the infinite tower of evolution equations for N -point correlation functions. Since the continuity and Euler equations of classical fluid dynamics relate the time derivative of the N -point function to the $(N+1)$ -point function, the power spectrum

$P(\vec{k})$ depends upon the bispectrum $B(\vec{k}_1, \vec{k}_2, \vec{k}_3)$, the bispectrum upon the trispectrum, and so on. Time-RG truncates this hierarchy by neglecting the connected part of the trispectrum, allowing the bispectrum to describe the non-linear evolution of the power spectrum.

Time-RG results were compared with those from N-body simulations in [44, 46]. In particular, Ref. [46] showed that Time-RG accurately predicted the power spectrum even for early dark energy models which cause Standard Perturbation Theory to fail, and for massive neutrino models to which other perturbative treatments are inapplicable. Furthermore, Time-RG was used to test the approximation of Refs. [47, 48], in which neutrino clustering is neglected as a source for non-linear dark matter growth.

In this article, we extend Time-RG to a prediction of the redshift-space power spectrum using the approach of Ref. [39], which describes higher-order corrections to the redshift-space power spectrum in terms of integrals $P_B(k, \mu)$ and $P_T(k, \mu)$ over the bispectrum and trispectrum, respectively. In particular, we show that $P_B(k, \mu)$ can be expressed as a linear combination of terms depending on k alone, whose time-evolution can be computed in the Time-RG framework. Our treatment automatically includes corrections to P_B due to non-linear evolution, and we show that these corrections result in a smearing of baryon oscillations in the P_B terms as well as a transfer in power from larger to smaller scales. Extending this calculation to massive neutrino models, we show that $\sum m_\nu$ and the equation of state parameters affect the redshift-space power spectrum differently, due to the scale-dependent growth sourced by massive neutrinos.

Next, we compare our calculations of the redshift-space power spectrum to the results of the HACC high-precision N-body simulations [49] used in Ref. [46]. For models without massive neutrinos, we show that the Time-RG predictions remain accurate down to smaller scales than those of Ref. [39], largely due to the better small-scale behavior of Time-RG relative to closure perturbation theory. Finally, we demonstrate that our approach accurately computes the redshift-space power spectrum for the full range of $\sum m_\nu$ allowed by current data [1, 50], and for models with cosmological constants as well as rapidly-varying dark energy.

This article is organized as follows. Section II covers Time-RG perturbation theory, the linear neutrino approximation used here, and the basics of perturbative RSD calculations. Our new results are derived in Sec. III, and after comparing them with the calculations of [39] we contrast the effects of $\sum m_\nu$ and the equation of state parameters on the redshift-space power spectrum. N-body simulations are used to test our results in Sec. IV. Section V concludes that our redshift-space Time-RG calculation agrees closely with N-body simulations in massive neutrino and evolving dark energy cosmologies, and discusses possible applications.

II. BACKGROUND

A. Time-RG Perturbation Theory

Consider a spatially-flat universe containing several non-relativistic fluids, each with density $\rho_I(\tau, \vec{x})$ and velocity field $\vec{v}_I(\tau, \vec{x})$, where τ and \vec{x} are the conformal time and comoving position, respectively. [70] Assume that the fluids interact only gravitationally. In terms of the density contrasts $\delta_I(\tau, \vec{x}) = \rho_I(\tau, \vec{x})/\bar{\rho}_I(\tau) - 1$, where the $\bar{\rho}_I(\tau)$ are the mean densities, we can write down the continuity and Euler equations for each fluid as well as a Poisson equation coupling them:

$$\frac{\partial \delta_I}{\partial \tau} + \vec{\nabla} \cdot \vec{v}_I + \vec{\nabla} \cdot (\vec{v}_I \delta_I) = 0 \quad (1)$$

$$\frac{\partial \vec{v}_I}{\partial \tau} + \mathcal{H} \vec{v}_I + (\vec{v}_I \cdot \vec{\nabla}) \vec{v}_I + \vec{\nabla} \Phi = 0 \quad (2)$$

$$\nabla^2 \Phi - \frac{3}{2} \Omega_m(\tau) \mathcal{H}^2 \sum_J f_J \delta_J = 0 \quad (3)$$

where the total cold matter density $\rho_m = \sum_J f_J \rho_J$. Here Φ is the gravitational potential and $\mathcal{H} = a^{-1} da/d\tau$ the conformal Hubble rate. In the regime of validity of cosmological perturbation theory, the velocity fields are well-approximated as irrotational, $\vec{\nabla} \times \vec{v}_i = 0$. Then each velocity can be described completely by its divergence $\theta_I = \mathcal{H}^{-1} \vec{\nabla} \cdot \vec{v}_i$ using $\nabla^2 \vec{v}_I = \mathcal{H} \vec{\nabla} \theta_I$. Henceforth we describe each fluid in terms of these scalar perturbations δ_I and θ_I .

We may put the equations of motion into a more compact notation. Let $\eta = \log[(1+z_{\text{in}})/(1+z)]$, where $z_{\text{in}} \gg 1$ is an initial redshift at which non-linear terms in the equations of motion are negligible. Working in redshift space, define $\varphi_{I0} = \exp(-\eta) \delta_I$ and $\varphi_{I1} = -\exp(-\eta) \theta_I$. With primes ($'$) denoting derivatives with respect to η , and summation over repeated lower-case indices, we have

$$\varphi'_{Ia} + \Omega_{Iab} \varphi_{Ib} = e^\eta \int \frac{d^3 q}{(2\pi)^3} \frac{d^3 p}{(2\pi)^3} \gamma_{abc}(\vec{k}, -\vec{p}, -\vec{q}) \quad (4)$$

$$\times \varphi_{Ib}(\vec{p}) \varphi_{Ic}(\vec{q}) (2\pi^3) \delta_D^3(\vec{k} + \vec{p} + \vec{q}) \quad (5)$$

$$\Omega_{I00} = -\Omega_{I01} = 1 \quad (6)$$

$$\Omega_{I10} = -\frac{3}{2} \Omega_m(\eta) \left(f_I + \sum_{J \neq I} f_J \frac{\delta_J}{\delta_I} \right) \quad (7)$$

$$\Omega_{I11} = 2 + \mathcal{H}'/\mathcal{H} \quad (8)$$

$$\gamma_{001}(\vec{k}, \vec{q}, \vec{p}) = \gamma_{010}(\vec{k}, \vec{p}, \vec{q}) = (\vec{p} + \vec{q}) \cdot \vec{q} / (2p^2) \quad (9)$$

$$\gamma_{111}(\vec{k}, \vec{q}, \vec{p}) = (\vec{p} + \vec{q})^2 \vec{p} \cdot \vec{q} / (2p^2 q^2) \quad (10)$$

with all other γ_{abc} zero. In the first line, the \vec{k} -dependence of φ on the left-hand-side has been suppressed, and δ_D is the Dirac delta function.

Next consider a universe with a single fluid. Using Eq. (4), Time-RG Perturbation Theory [41] writes down the equations of motion for the power spectrum $P_{ab}(\vec{k}_1)(2\pi)^3 \delta_D^3(\vec{k}_1 + \vec{k}_2) = \langle \varphi_a(\vec{k}_1) \varphi_b(\vec{k}_2) \rangle$ and

Model	h	ω_m	ω_b	ω_ν	n_s	σ_8	w_0	w_a
Λ CDM	0.71	0.1335	0.02258	0	0.963	0.8	-1	0
$\nu\Lambda$ CDM	0.71	0.1335	0.02258	0.001	0.963	0.8	-1	0
EDE	0.6167	0.1472	0.02261	0	0.9611	0.8778	-0.7	0.6722
ν wCDM	0.7342	0.1543	0.02323	0.003	0.8797	0.8056	-1.21	-1.11

TABLE I: List of cosmological models considered here. For each component J , $\omega_J = \Omega_J(\tau_0)h^2$, where τ_0 is the time today.

bispectrum $B_{abc}(\vec{k}_1, \vec{k}_2, \vec{k}_3)(2\pi^3)\delta_D^3(\vec{k}_1 + \vec{k}_2 + \vec{k}_3) = \langle \varphi_a(\vec{k}_1)\varphi_b(\vec{k}_2)\varphi_c(\vec{k}_3) \rangle$:

$$P'_{ab} = -\Omega_{ac}P_{cb}(k) - \Omega_{bc}P_{ac}(k) + e^\eta \int \frac{d^3q}{(2\pi)^3} [\gamma_{acd}(k, q, p)B_{bcd}(k, q, p) + \gamma_{bcd}(k, q, p)B_{acd}(k, q, p)] \quad (10)$$

$$B'_{abc} = -\Omega_{ad}(k)B_{dbc} - \Omega_{bd}(q)B_{adc} - \Omega_{cd}(p)B_{abd} + 2e^\eta [\gamma_{ade}(k, q, p)P_{db}(q)P_{ec}(p) + \gamma_{bde}(q, p, k)P_{dc}(p)P_{ea}(k) + \gamma_{cde}(p, k, q)P_{da}(k)P_{eb}(q)] \quad (11)$$

where the bispectrum in the second equation is understood to be a function of k , q , and p : $B_{abc} = B_{abc}(k, q, p)$.

Needing to keep track of the functional dependence of B_{abc} on three different variables would make Time-RG perturbation theory numerically prohibitive. However, it is possible to recast the equations of motion in such a way that the time-dependent quantities depend only on one variable, k :

$$P'_{ab} = -\Omega_{ac}P_{bc} - \Omega_{bc}P_{ac} + e^\eta \frac{4\pi}{k} (I_{acd,bcd} + I_{bcd,acd}) \quad (12)$$

$$\frac{I_{acd,bef}}{k} = \int \frac{q^2 dq \sin \alpha d\alpha}{(2\pi)^3} \frac{\gamma_{acd}(k, q, p_-)B_{bef}(k, q, p_-)}{2} \quad (13)$$

$$I'_{acd,bef} = -\Omega_{bg}I_{acd,gef} - \Omega_{eg}I_{acd,bgf} - \Omega_{fg}I_{acd,beg} + 2e^\eta A_{acd,bef} \quad (14)$$

$$\frac{A_{acd,bef}}{k} = \int \frac{q^2 dq \sin \alpha d\alpha}{(2\pi)^3} \frac{\gamma_{acd}(k, q, p_-)}{2} \times \left[\gamma_{bgh}(k, q, p_-)P_{ge}(q)P_{hf}(p_-) + \gamma_{egh}(q, p_-, k)P_{gf}(p_-)P_{hb}(k) + \gamma_{fgh}(p_-, k, q)P_{gb}(k)P_{he}(q) \right]. \quad (15)$$

Here, $\vec{p}_\pm = \vec{k} \pm \vec{q}$, and the P_{ab} , $I_{acd,bef}$, and $A_{acd,bef}$ depend on k unless otherwise specified. Since most of the γ_{abc} are zero, there are only 24 nonzero components of $I_{acd,bef}$ at each k , only 14 of which are independent.

Before proceeding, we note that the treatment of nonlinearities in Eq. (14) neglects any scale-dependence in Ω . In particular, in a cosmological model containing multiple species which cluster differently, such as cold dark matter and massive neutrinos, Ω_{10} will depend on k as

given by Eq. (6). Since this is a small correction to a non-linear correction, it is expected to be small [51], and it will be further suppressed when the density fraction of the second species is small. We defer discussion of the scale dependence of Eq. (14) and its redshift-space generalization to Appendix C, in which we show that the associated error is less than 1% all the way to $z = 0$ and $k = 0.4 h/\text{Mpc}$ even for neutrino masses $\sum m_\nu = 0.94 \text{ eV}$ much larger than current bounds.

The Time-RG calculations of Eqs. (12-15) may be sped up considerably by replacing the power spectra inside the integral of Eq. (15) by the linear-theory power spectra. Since these scale in a known way with the growth factor $D(z)$ and its logarithmic derivative $f(z) = -d \log D / d \log(1+z)$, the integral need not be repeated at each time step. This is known as the ‘‘1-loop’’ approximation of Time-RG, since it is equivalent to standard perturbation theory at the 1-loop level [41]. On a standard 8-core desktop computer, 1-loop Time-RG and other 1-loop computations take ~ 1 minute, full Time-RG takes ~ 1 hour, and 2-loop perturbation theories take ~ 1 day to compute the power spectrum over 100 k values in the range $0.001 h/\text{Mpc} \leq k \leq 1 h/\text{Mpc}$.

Figures 1 and 2 show our results for a massless-neutrino model with cosmological constant (Λ CDM) and an early dark energy model (EDE) whose parameters are given in Table I; power spectra have been divided by the ‘‘no-wiggle’’ power spectrum $P_{\text{nw}}(k)$ of Ref. [52]. Time-RG is compared to the N-body simulations of Ref. [46], as well as to the 1- and 2-loop closure theory calculations of Refs. [53–55] implemented in the `Copter` code [44]. Full and 1-loop Time-RG are very similar in this range of k , with the 1-loop power spectrum slightly larger at $k \gtrsim 0.25 h/\text{Mpc}$. While 2-loop closure theory is highly accurate, its computation time makes it difficult to use in an analysis exploring a large parameter space. Meanwhile, 1-loop closure theory is comparable to 1-loop Time-RG in accuracy as well as running time in the $k \leq 0.2 h/\text{Mpc}$ range. Although all perturbative calculations break down for sufficiently large k , one advantage of Time-RG is that it diverges relatively slowly from N-body calculations, remaining within $\approx 10\%$ of the N-body power spectrum up to $k = 0.3 h/\text{Mpc}$ for $z \geq 0.5$ in both figures. Figure 3, a comparison to the high-resolution Λ CDM N-body simulation of Ref. [46], shows that both versions of Time-RG are correct in the range $k \leq 1 h/\text{Mpc}$ to $< 10\%$ for $z \geq 1$ and to $< 5\%$ for $z \geq 2$. The figure also shows two other trends: first, that full and 1-loop Time-RG differ substantially only for $k \gtrsim 1 h/\text{Mpc}$; and, second, that full Time-RG underestimates the small-scale power at high z while overestimating it at low z . Figure 4 compares Time-RG to the velocity power spectrum $P_{\theta\theta}$ and the cross spectrum $P_{\delta\theta}$. Since the velocity field can only be determined to scales $k \approx 0.5 h/\text{Mpc}$ given our simulation resolution, we truncate the figure there. Evidently Time-RG is accurate at the 10% level to $k = 0.3 h/\text{Mpc}$ for both power spectra. It is not quite as accurate as it was for the density power

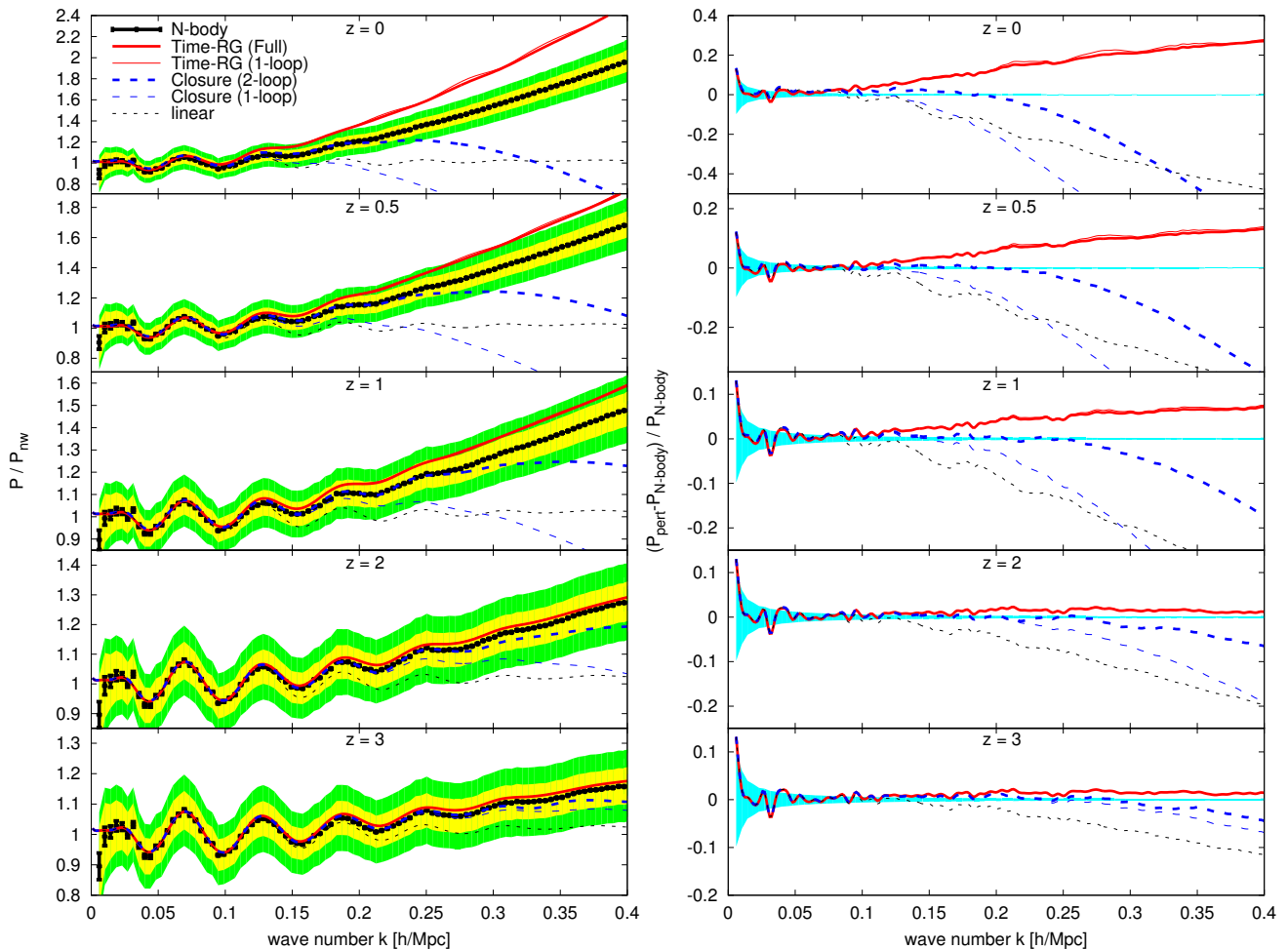


FIG. 1: Power spectrum $P_{\delta\delta}$ for the model Λ CDM. (Left) Points with error bars show the N-body simulations of Ref. [46], and the inner (outer) shaded regions are within 5% (10%) of the simulation points. Full and 1-loop Time-RG are compared with the closure theory calculations of Ref. [39]. Note that at the wave numbers shown, full and 1-loop Time-RG are indistinguishable except at $z = 0$ and $k \gtrsim 0.25 h/\text{Mpc}$. (Right) Fractional errors associated with the perturbation theories on the left. The shaded region shows the 2σ N-body simulation error bars.

spectrum, but once again, Time-RG diverges from the N-body spectra smoothly.

We conclude by addressing an error in the original Time-RG algorithm [41]. As noted above, there are 14 independent components of the $A_{acd,bef}(k)$ integral at each k ; however, the original work included only 12 of them, as pointed out in Ref. [56]. The erroneous version was implemented in *Copter*, and Ref. [44] reported a discrepancy between simulations and the Time-RG predictions of the density-velocity cross-spectrum as well as the velocity auto-spectrum. In Figure 5, we add the corrected Time-RG power spectra to their figure. Including all of the $A_{acd,bef}$ increases $P_{\delta\theta}$ and $P_{\theta\theta}$, improving agreement with simulations in the $k < 0.1 h/\text{Mpc}$ region. This is significant because the velocity power spectra are important to calculations of the redshift-space power.

B. Massive neutrinos: Linear approximation

The coupled system of equations for multiple, non-linear, non-interacting fluids was described in Sec. II A. Since baryonic gas dynamics and feedback effects are only important at small scales, beyond the reach of perturbation theory, we regard the cold dark matter (CDM) and baryons as one single fluid, labelled “CB.” We also consider a second fluid “ ν ” consisting of three equal-mass neutrino species, which behave as a warm dark matter component. Though a generalization to more neutrino species of different masses is straightforward, we focus on the simplest case here. Henceforth a subscript “m” refers to CDM, baryons, and neutrinos together, so that $\Omega_m = \Omega_{\text{CDM}} + \Omega_b + \Omega_\nu$. The sum of neutrino masses is related to the neutrino density fraction $\omega_\nu = \Omega_{\nu,0} h^2$ by $\sum m_\nu = 94\omega_\nu$ eV.

Since neutrinos do not cluster strongly, they can further be approximated as a purely linear fluid in Time-RG

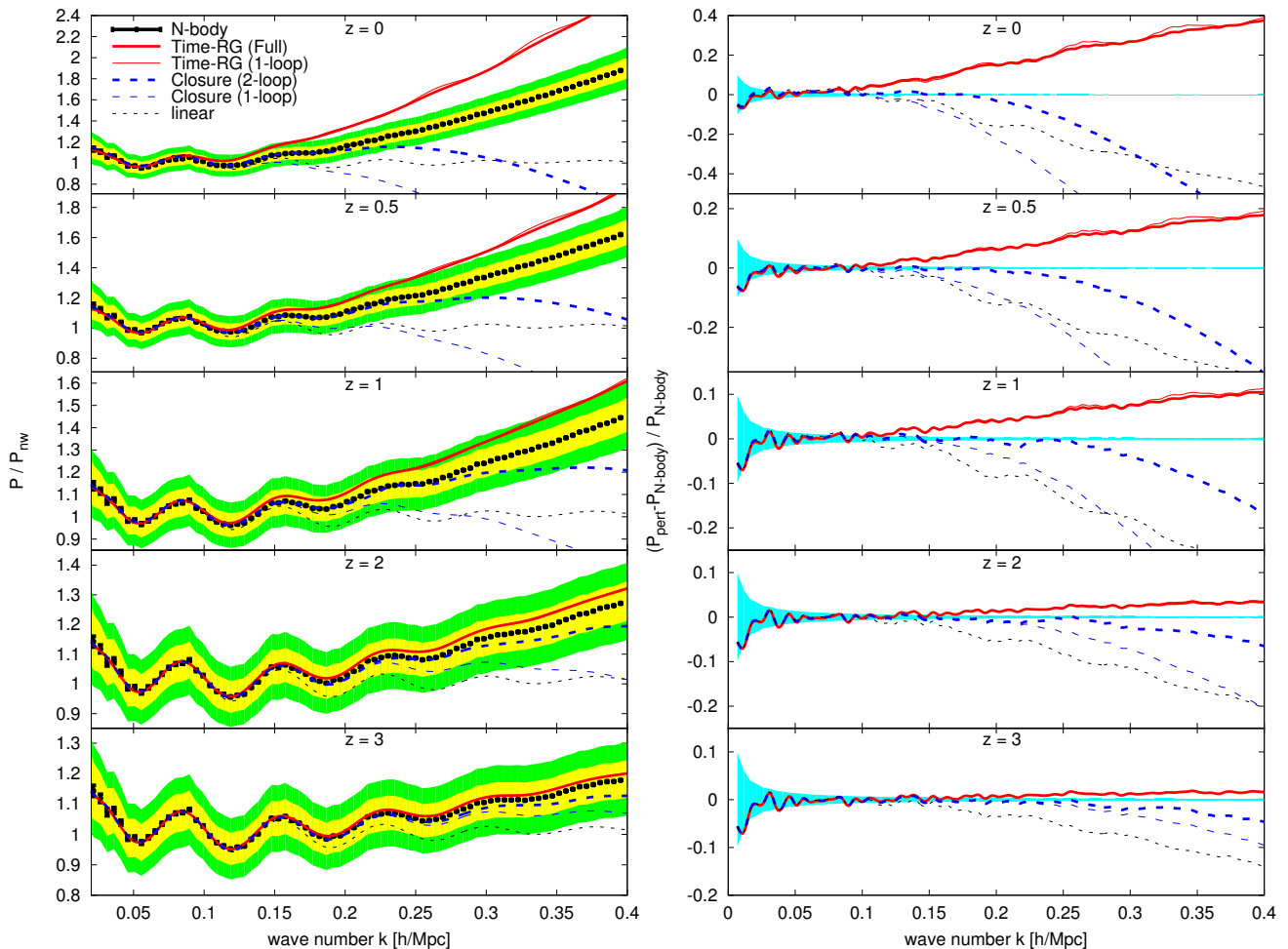


FIG. 2: Same as Figure 1, but for the early dark energy model EDE from Table I.

perturbation theory [41, 42]. Thus we may use a linear code such as CAMB or CMBFAST [57–59] to compute the coupling matrix Ω_{CB} . Dropping the “CB” subscript of Ω , we have

$$\Omega_{10} \approx -\frac{3}{2}\Omega_{\text{m}}(\eta) [f_{\text{CB}} + \mathcal{B}_{\nu}(\eta, k)] \quad (16)$$

$$\mathcal{B}_{\nu} = f_{\nu} \delta_{\text{lin},\nu} / \delta_{\text{lin,CB}}. \quad (17)$$

Using $\delta_{\text{lin,CB}}$ rather than δ_{CB} in the denominator of \mathcal{B}_{ν} makes only a negligible difference [42]. Non-linear evolution of δ_{ν} is also not the dominant source of error in this approximation [51, 60, 61]. Thus Time-RG can incorporate massive neutrinos, or other species leading to scale-dependent CB growth, without much difficulty.

In the two-fluid case, the total matter perturbation is $\delta_{\text{m}} = (\bar{\rho}_{\text{CB}}\delta_{\text{CB}} + \bar{\rho}_{\nu}\delta_{\nu}) / \bar{\rho}_{\text{m}} = f_{\text{CB}}\delta_{\text{CB}} + f_{\nu}\delta_{\nu}$. In the linear neutrino approximation, the non-linear matter power spectrum is given by

$$P_{\text{m}}(k) \approx f_{\text{CB}}^2 P_{\text{CB}} + 2f_{\text{CB}}f_{\nu} \sqrt{P_{\text{CB}}P_{\text{lin},\nu}} + f_{\nu}^2 P_{\text{lin},\nu}. \quad (18)$$

Figure 6 compares P_{CB} , $P_{\text{lin},\nu}$, and $\sqrt{P_{\text{CB}}P_{\text{lin},\nu}}$ to the linear CB power spectrum.

Based on the figure, the linear-neutrino approximation should apply even beyond the quasi-linear regime $k \sim 0.1 h/\text{Mpc}$. Non-linear effects in each fluid become important when $\Delta_{\text{lin}}^2 \sim 1$, as seen by comparing the $\text{CB} \times \text{CB}$ and linear curves. Even for a rather large neutrino mass at $z = 0$, the neutrino auto-spectrum remains below 0.1, while the cross-spectrum plateaus around 0.25. If $\Delta_{\nu}^2(k) - \Delta_{\text{lin},\nu}^2(k) \sim \Delta_{\text{lin},\nu}^4(k)$, then the leading-order fractional correction to Eq. (18) will be $\sim (f_{\nu}/f_{\text{CB}}) \sqrt{\Delta_{\text{lin},\nu}^2 / \Delta_{\text{CB}}^2 \Delta_{\text{lin},\nu}^2}$, which is at most $\sim 1\%$. Moreover, non-linear corrections to Δ_{ν}^2 should diminish in importance for $k \gg 0.1 h/\text{Mpc}$, allowing a variant of this approximation to be used even in N-body simulations [46, 48].

C. Redshift-space distortions

In a perfectly homogeneous universe, there is a precise relation between the redshift z of an object and the comoving distance $\chi(z) = \int_0^z dz'/H(z')$ to that object. Peculiar velocities \vec{v} sourced by density inhomom-

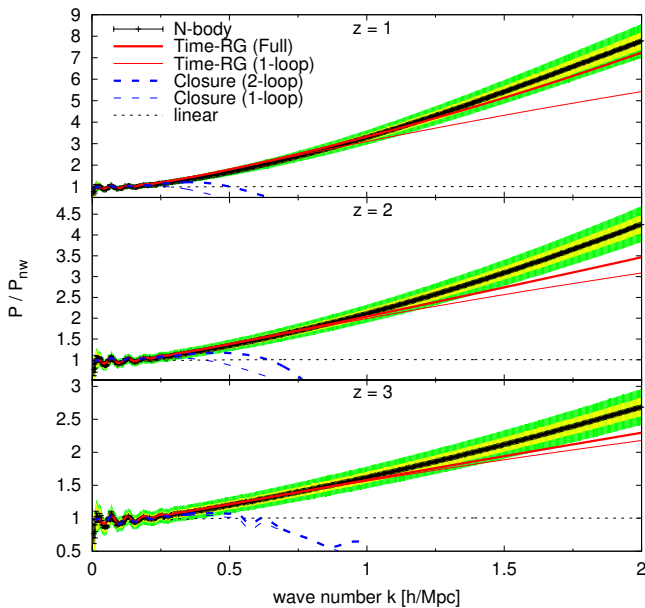


FIG. 3: Same as Figure 1, but using the high-resolution TreePM simulation of [46], accurate to much smaller scales.

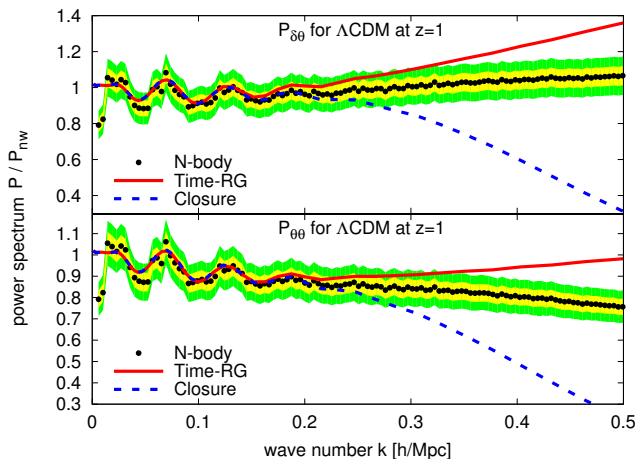


FIG. 4: Density-velocity cross spectrum $P_{\delta\theta}$ and velocity power spectrum $P_{\theta\theta}$ at $z=1$ for Λ CDM. Inner and outer shaded regions correspond to 5% and 10% deviations, respectively, from the N-body points.

genities δ distort this relation, perturbing χ in the line-of-sight direction \hat{r} by an amount $\vec{v} \cdot \hat{r} / \mathcal{H}$ (where \hat{r} denotes a unit vector). If the homogeneous-universe relation is used to identify redshift z with position $\chi(z)$ (“redshift space”), then this peculiar-velocity effect shows up as a direction-dependent distortion of the power spectrum. Such redshift-space distortions (RSD) enhance the line-of-sight power spectrum in the quasi-linear regime (“squashing”) and suppress it in the non-linear regime (“fingers of god”) [62].

A discussion of linear RSD as given in Ref. [37] is instructive. A volume element at comoving position \vec{x} and redshift z , at which point the velocity field takes the

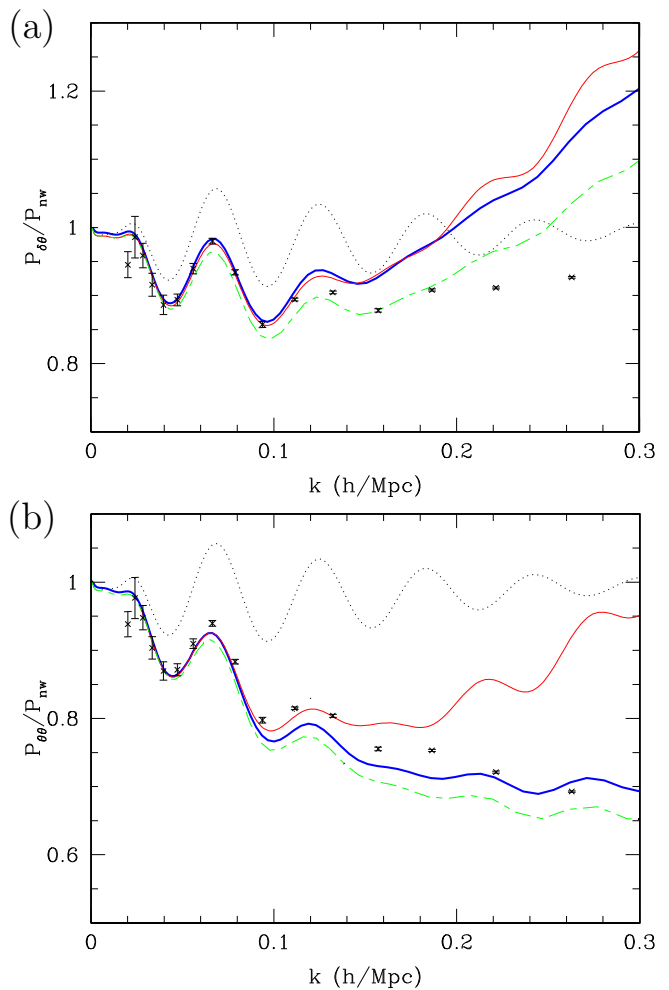


FIG. 5: (a) Velocity-density cross-spectrum and (b) velocity auto-spectrum for the Λ CDM model of Ref. [44] at $z = 0$. Black points are their N-body simulation, and the solid (red) line is 1-loop Standard Perturbation Theory. Properly including all of the $A_{acd,bef}$ integrals of Eq. (15) in the Time-RG calculation leads to an improved fit (solid blue line) at low k relative to the Time-RG results of Refs. [41, 44] (dot-dashed green line). Adapted from Figure 8 of Ref. [44].

value $\vec{v}(z, \vec{x})$, will be assigned a redshift-space position $\vec{x}_s = \vec{x} + \hat{x} \vec{v} \cdot \hat{x} / \mathcal{H}$. For example, an object falling toward the observer ($\vec{v} \cdot \hat{x} < 0$) will appear closer ($|\vec{x}_s| < |\vec{x}|$) in redshift space than in real space. In the flat-sky approximation, $\hat{x} \approx \hat{r} = \text{constant}$, and the Jacobian determinant associated with the transformation from real- to redshift-space is $J = |d^3x/d^3x_s| = (1 + \partial_x \vec{v} \cdot \vec{r} / \mathcal{H})^{-1}$.

Since the total number of objects (or the total mass) in a given volume does not depend on the coordinates that we use, we can relate the redshift-space overdensity δ_s to the real-space overdensity by $1 + \delta_s = (1 + \delta)J$. In Fourier space, for an irrotational velocity field $\vec{v}(\vec{k}) \propto \vec{k}$, this becomes $\delta_s = (\delta + \mu_{\vec{k}}^2 \theta)J$, where $\mu_{\vec{k}} = \hat{k} \cdot \hat{r}$. In linear

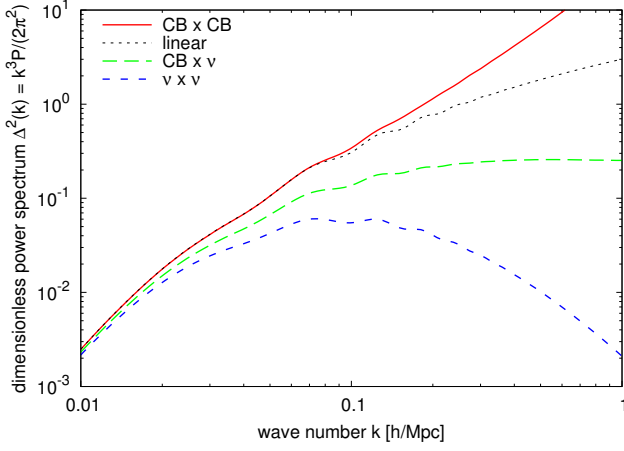


FIG. 6: Dimensionless power spectra $\Delta^2(k) = \frac{k^3}{2\pi^2}P(k)$ for a $\omega_\nu = 0.01$ ($\sum m_\nu = 0.94$ eV) model at $z = 0$. The cross-spectrum $P_{\text{CB} \times \nu} \approx \sqrt{P_{\text{CB}} P_{\text{lin}, \nu}}$ and the neutrino auto-spectrum $P_\nu \approx P_{\text{lin}, \nu}$ use the linear-neutrino approximation.

theory, $\delta_s \approx (1 + f\mu_{\vec{k}}^2)\delta$, implying the power spectrum

$$P_{s, \text{lin}}(k, \mu_{\vec{k}}) = (1 + f\mu_{\vec{k}}^2)^2 P_{\text{lin}}(k). \quad (19)$$

This qualitatively describes line-of-sight power enhancement expected due to large-scale infall towards matter overdensities, but does not include finger-of-god effects at smaller scales.

In order to extend such a treatment beyond linear theory, two types of corrections have been introduced: streaming models and higher-order corrections to the power spectrum [40, 63]. The simplest higher-order correction is to replace P_{lin} in Eq. (19) by the non-linear density power spectrum, while the Scoccimarro ansatz [38] replaces all three linear power spectra with their non-linear equivalents in order to damp the redshift-space power spectrum:

$$P_s(k, \mu_{\vec{k}}) = P_{\delta\delta} + 2\mu_{\vec{k}}^2 P_{\delta\theta} + \mu_{\vec{k}}^4 P_{\theta\theta}. \quad (20)$$

All of these non-linear corrections essentially try to reduce the amplitude of the linear redshift space power spectrum to mimic the effect of non-linear structure formation.

Streaming models explicitly impose finger-of-god suppression by multiplying $P_s(k, \mu_{\vec{k}})$ by a function $F_{\text{fog}}(fk\sigma_v\mu_{\vec{k}})$, which typically takes a simple form:

$$F_{\text{fog}}(x) = \begin{cases} \exp(-x^2) & \text{(Gaussian)} \\ (1+x^2)^{-1} & \text{(Lorentzian)}. \end{cases} \quad (21)$$

Here $3\sigma_v^2$ is the trace of the velocity-dispersion tensor. In practice, it is either fit to the data at each z , or approximated by its linear-theory value

$$\sigma_{v, \text{lin}}^2 = \frac{1}{3} \int \frac{d^3k}{(2\pi)^3} P_{vv} = \frac{f^2 \mathcal{H}^2}{6\pi^2} \int dk P_{\text{lin}}(k) \quad (22)$$

where P_{lin} is the linear matter power spectrum. The convention in the literature is to “absorb” the $f^2 \mathcal{H}^2$ into the σ_v^2 , so that typical values of $\sigma_{v, \text{lin}} = \sqrt{\int P_{\text{lin}} dk / (6\pi^2)}$ for a Λ CDM model at $z \sim 1$ are ~ 1 Mpc/h.

The treatments above approximate the redshift-space power spectrum in terms of the real-space power spectra. From the form of the Jacobian it is clear that higher-order correlation functions ought to play a role; however, the gradient term in the denominator of J suggests that a simple Taylor expansion will be badly-behaved when $\theta \sim 1$. Instead, Ref. [38] uses spatial homogeneity to derive an exact formula for P_s without a badly-behaved Jacobian denominator:

$$P_s(\vec{k}) = \int d^3x e^{i\vec{k}\cdot\vec{x}} \left\langle e^{-i\vec{k}\cdot\hat{r}\Delta u} \left[\delta(\vec{y}) + (\hat{r} \cdot \vec{\nabla})u(\vec{y}) \right] \times \left[\delta(\vec{y}') + (\hat{r} \cdot \vec{\nabla})u(\vec{y}') \right] \right\rangle \quad (23)$$

where $u(\vec{y}) = -\vec{v}(\vec{y}) \cdot \hat{r} / \mathcal{H}$, $\Delta u = u(\vec{y}) - u(\vec{y}')$, and $\vec{x} = \vec{y} - \vec{y}'$. Recognizing that the Kaiser “squashing” and finger-of-god effects are coupled and cannot be treated separately, Taruya, Nishimichi, and Saito (TNS [39]) apply a cumulant expansion to the expectation value in Eq. (23) and find a series of corrections to P_s in terms of higher-order correlation functions. The leading-order corrections are obtained by neglecting all higher-order correlation functions except for the bispectrum and the disconnected parts of the trispectrum, precisely the approximation used in Time-RG:

$$P_s(k, \mu) = F_{\text{fog}}(f\sigma_v k \mu) [P_{\delta\delta}(k) + 2\mu^2 P_{\delta\theta}(k) + \mu^4 P_{\theta\theta}(k) + P_{\text{B}}(k, \mu) + P_{\text{T}}(k, \mu)] \quad (24)$$

$$\frac{P_{\text{B}}(k, \mu)}{k\mu} = \int \frac{d^3q}{(2\pi)^3} \frac{\mu_{\vec{q}}}{q} \left[B_{\text{TNS}}(\vec{q}, \vec{k} - \vec{q}, -\vec{k}) - B_{\text{TNS}}(\vec{q}, \vec{k}, -\vec{k} - \vec{q}) \right] \quad (25)$$

$$\frac{P_{\text{T}}(k, \mu)}{k^2 \mu^2} = \int \frac{d^3q}{(2\pi)^3} \tau_{\text{TNS}}(\vec{q}) \tau_{\text{TNS}}(\vec{k} - \vec{q}) \quad (26)$$

$$B_{\text{TNS}}(\vec{k}_1, \vec{k}_2, \vec{k}_3) = B_{\theta\delta\delta}(\vec{k}_1, \vec{k}_2, \vec{k}_3) - \mu_{\vec{k}_2}^2 B_{\theta\theta\delta}(\vec{k}_1, \vec{k}_2, \vec{k}_3) - \mu_{\vec{k}_3}^2 B_{\theta\theta\delta}(\vec{k}_1, \vec{k}_2, \vec{k}_3) + \mu_{\vec{k}_2}^2 \mu_{\vec{k}_3}^2 B_{\theta\theta\theta}(\vec{k}_1, \vec{k}_2, \vec{k}_3) \quad (27)$$

$$\tau_{\text{TNS}}(\vec{k}_1) = \frac{\mu_{\vec{k}_1}}{k_1} \left[P_{\delta\theta}(\vec{k}_1) + \mu_{\vec{k}_1}^2 P_{\theta\theta}(\vec{k}_1) \right] \quad (28)$$

Here and henceforth, μ is assumed to mean $\mu_{\vec{k}}$ unless otherwise labelled. A thorough study of approximations to P_s finds this approach to be the most successful at matching N-body calculations and at providing an unbiased estimate of the growth rate f [40].

In practice, Ref. [39] computes the power spectra in Eq. (24) using closure theory, the bispectra in Eq. (25) using the tree-level approximation of Ref. [64], and the power spectra in Eq. (26) using linear theory. In the next

Section, we compute all of these terms together in Time-RG perturbation theory, making only the standard Time-RG approximation of neglecting the connected trispectrum. There are three potential advantages to this approach:

1. Time-RG is easily-generalized to multi-component models with scale-dependent growth;
2. Time-RG is well-behaved at $k \lesssim 1 h/\text{Mpc}$ for $z \gtrsim 1$, with errors $\lesssim 10\%$; and
3. errors may be estimated by approximating the connected trispectrum, as in Ref. [56].

Regarding the second of these, the most promising perturbative RSD treatments employ a streaming function F_{fog} , a phenomenological model which is not expected to be correct beyond the $\approx 5\%$ level at quasi-linear scales $k \gtrsim 0.1 h/\text{Mpc}$. Thus percent-level accuracy in the computation of the power spectra is unnecessary; much more important is the calculation of $P(k)$ at the 5% – 10% level over a larger range of scales.

III. REDSHIFT-SPACE DISTORTIONS IN TIME-RG PERTURBATION THEORY

A. P_B and P_T in Time-RG

Further analysis can substantially simplify the computation of P_B and P_T . Though we defer the details to Appendices A and B, we summarize the results here. First, the μ -dependence of $P_s(k, \mu)$ can be separated out, yielding a polynomial in μ^2 with k -dependent coefficients:

$$P_s(k, \mu) = F_{\text{fog}}(f\sigma_v k\mu)[P_0(k) + P_2(k)\mu^2 + P_4(k)\mu^4 + P_6(k)\mu^6 + P_8(k)\mu^8]. \quad (29)$$

Both P_B and P_T contribute to P_2 , P_4 , and P_6 , while P_T also contributes to P_8 :

$$\begin{aligned} P_B(k, \mu) &= P_{B,2}(k)\mu^2 + P_{B,4}(k)\mu^4 + P_{B,6}(k)\mu^6 \quad (30) \\ P_T(k, \mu) &= P_{T,2}(k)\mu^2 + P_{T,4}(k)\mu^4 \\ &\quad + P_{T,6}(k)\mu^6 + P_{T,8}(k)\mu^8. \quad (31) \end{aligned}$$

Second, rather than keeping track of the full functional dependence of the bispectrum in order to integrate Eq. (25) for the $P_{B,j}$, we can break up the bispectrum integrals into a series of terms $Q_{abc}^{(\ell)}$, with $-1 \leq \ell \leq 3$, which depend only on k and η . In the Time-RG framework, the evolution equations for the $Q_{abc}^{(\ell)}$ follow from Eq. (11). Thus the $Q_{abc}^{(\ell)}$ are analogous to the $I_{acd,bef}(k)$ in real-space Time-RG (13). Appendix A expresses the $P_{B,j}$ as linear combinations of $kQ_{abc}^{(\ell)}$ and then derives these evolution equations, which require the computation of a two-dimensional integral analogous to $A_{acd,bef}$

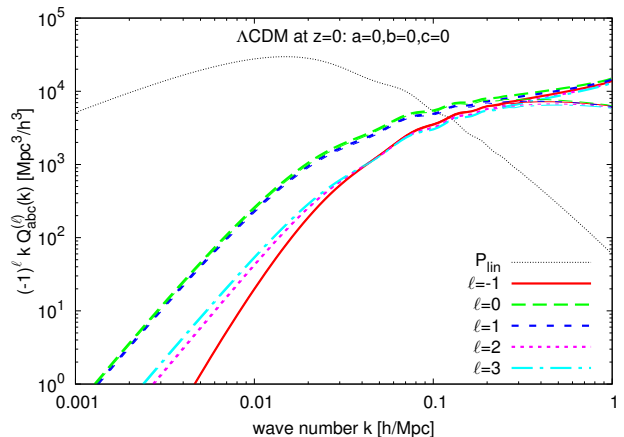


FIG. 7: Bispectrum integrals $(-1)^\ell k Q_{abc}^{(\ell)}(k)$ with $a = b = c = \delta$, for ΛCDM at $z = 0$. Thick lines show full Time-RG, while thin lines show its 1-loop approximation. The other components are similar in magnitude as well as k -dependence. The linear power spectrum is included for comparison.

at each time step. Figure 7 compares $kQ_{abc}^{(\ell)}$ to the linear power spectrum, showing that non-linear contributions to redshift-space distortions are non-negligible at the BAO scale. The figure also shows 1-loop approximations to $Q_{abc}^{(\ell)}$.

Meanwhile, computation of the $P_{T,j}$ is straightforward. We describe it in Appendix B for completeness, but the only change relative to Ref. [39] is that we carry out the computation using the non-linear power spectra.

The full set of evolution equations for redshift-space distortions in Time-RG perturbation theory is then Eqs. (12,13,14,15,A7,A8). Since the bispectra are small at early times, the $Q_{abc}^{(\ell)}$ can be initialized to zero, as with the $I_{acd,bef}$. Reference [51] finds that the resulting error is approximately $1/z_{\text{in}}$ for an initial redshift z_{in} , and our numerical results with $z_{\text{in}} = 200$ are consistent with this. Redshift-space Time-RG follows the 40 terms $Q_{abc}^{(\ell)}$ as well as 14 unique $I_{acd,bef}$, so we can expect a fourfold increase in computation time relative to real-space Time-RG. Our implementation of redshift-space Time-RG, **redTime**, is available on-line at <http://www.hep.anl.gov/cosmology/pert.html>. **redTime** uses the GNU Scientific Library [65] to evolve the equations of motion, and the CUBA Library [66] to compute numerically the multi-dimensional integrals in Eqs. (15,A8,B1). The redshift-space and multipole plots in this article have been produced using CAMB for transfer functions and **redTime** for Time-RG calculations.

B. Comparison to the literature

Figures 8 and 9 compare our calculations to those of Ref. [39] for a ΛCDM cosmology. The correction terms $P_{B,j}$ and $P_{T,j}$ are directly compared in Fig. 8, which

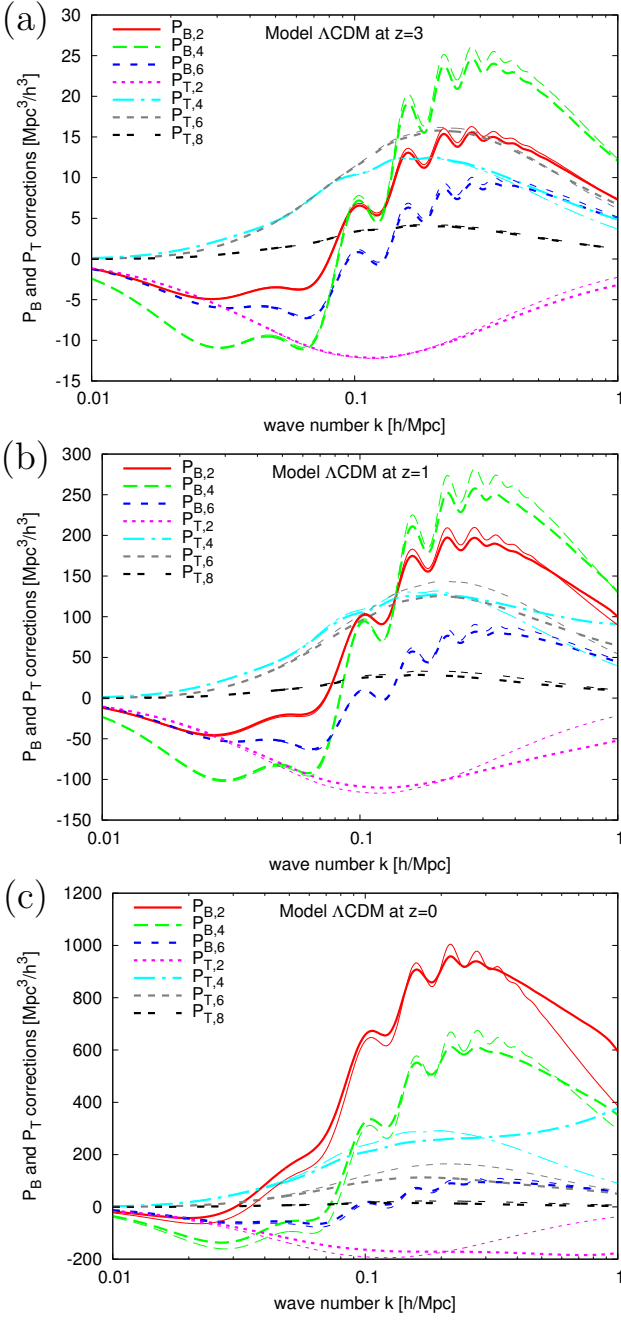


FIG. 8: Non-linear corrections $P_{B,j}(k)$ and $P_{T,j}(k)$ to the redshift-space power spectrum. Time-RG calculations are shown as thick lines, and the results of [39] are thin lines. ΛCDM is shown at: (a) $z = 3$; (b) $z = 1$; (c) $z = 0$.

shows that the two sets of results agree closely at early times and large scales. Ref. [39] predicts somewhat larger corrections at $k \leq 0.2 \text{ h}/\text{Mpc}$, while Time-RG corrections become larger in magnitude around $k \sim 1 \text{ h}/\text{Mpc}$.

Multipole moments of the redshift-space power spectrum $P_s(k, \mu)$ are found by projecting Eq. (24) onto a

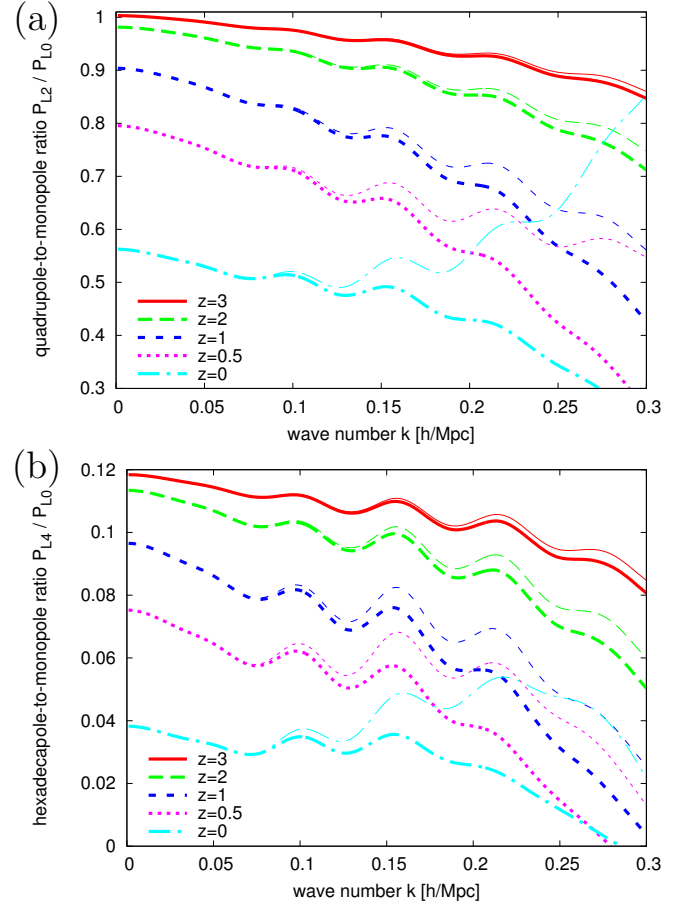


FIG. 9: Ratios of the (a) quadrupole and (b) hexadecapole to the monopole of the redshift-space power spectrum $P_s(k, \mu)$, shown for the model ΛCDM . Time-RG calculations are shown as thick lines and TNS calculations as thin lines, with σ_v taken from linear theory.

basis of Legendre polynomials $\mathcal{P}_\ell(\mu)$ for even ℓ :

$$P_{L,\ell}(k) = \frac{2\ell+1}{2} \int_{-1}^1 d\mu P_s(k, \mu) \mathcal{P}_\ell(\mu). \quad (32)$$

Defining $P_{L,\ell} = \sum_{j=0}^{\ell} \mathcal{M}_{\ell,2j} P_{2j}$, $m_n = \int_{-1}^1 d\mu \mu^{2n} F_{\text{fog}}$, $\alpha = fk\sigma_v$, and the Legendre coefficients $p_{\ell i}$ such that $\mathcal{P}_\ell(x) = \sum_i p_{\ell i} x^{2i}$ for even ℓ , we have $\mathcal{M}_{\ell,2j} = \frac{2\ell+1}{2} \sum_i p_{\ell i} m_{i+j}$. For a Gaussian $F_{\text{fog}}(\alpha\mu)$, $m_n^G = \gamma(\frac{2n+1}{2}, \alpha^2)/\alpha^{2n+1}$, where $\gamma(a, x) = \int_0^x e^{-t} t^{a-1} dt$ is the incomplete gamma function. For a Lorentzian F_{fog} , $m_0^L = 2\alpha^{-1} \arctan(\alpha)$, and for $n \geq 1$ we have the recursion relation $\alpha^2 m_n^L = 2/(2n-1) - m_{n-1}^L$.

Ratios of the quadrupole ($\ell = 2$) and hexadecapole ($\ell = 4$) to the monopole ($\ell = 0$) are shown in Fig. 9 for the Time-RG and TNS [39] calculations. At early times and large scales, the quadrupole and hexadecapole ratios approach their linear Einstein-de Sitter values $50/49$ and $6/49$, respectively. At smaller scales, Time-RG and TNS agree at early times, while TNS predicts substantially higher quadrupole-to-monopole and hexadecapole-

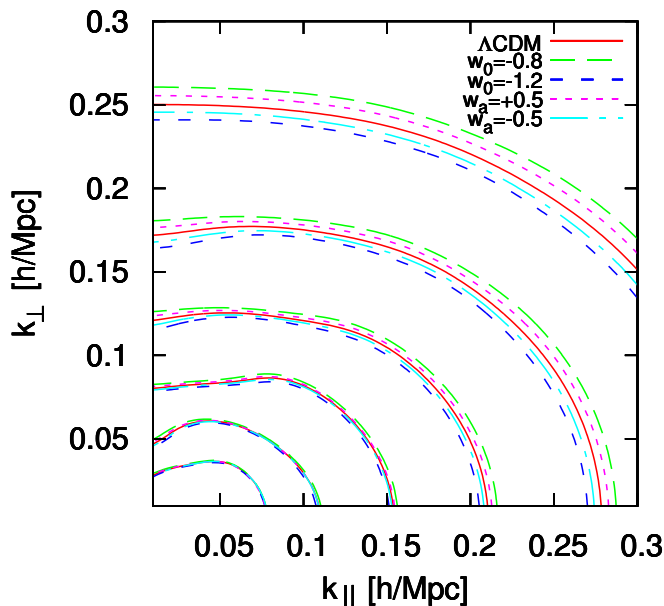


FIG. 10: Logarithmic contours of the redshift-space power spectrum $P_s(k_{\parallel}, k_{\perp})$ at $z = 1$. The equation of state parameters w_0 and w_a are varied from their Λ CDM values $w_0 = -1$, $w_a = 0$, with all other parameters held fixed.

to-monopole ratios at late times. This is due in part to the fact that Time-RG overestimates the late-time non-linear power spectrum $P_{\delta\delta}$, while the closure theory calculation of Ref. [39] underestimates it [44].

C. Redshift-space power spectrum

The two main aims of this article are to compute the effects of massive neutrinos and evolving dark energy on the redshift-space power spectrum $P_s(k_{\parallel}, k_{\perp})$, and to demonstrate that our results are consistent with N-body simulations. We are now in a position to do the first of these.

Figure 10 shows the redshift-space power spectrum for a range of dark energy models. As either w_0 or w_a is increased, leading to an overall increase in $w(z)$, the power spectrum increases both parallel and perpendicular to the line of sight. Effectively the perpendicular direction constrains the growth factor $D(z)$ while the μ -dependence of P_s constrains the derivative $f = -d \log D / d \log(1+z)$.

Meanwhile, Figure 11 varies the neutrino density fraction in Λ CDM models while keeping the early-time power spectrum normalization constant. The resulting variation in σ_8 , the late-time normalization, is the largest contributor to the differences among the power spectra in Fig. 11. Since Cosmic Microwave Background (CMB) measurements constrain the early-time normalization, neutrino constraints are strongest when CMB and large-scale structure data are combined [3].

Aside from differences in σ_8 , the models in Fig. 11 differ in their redshift-space dependence to a much greater

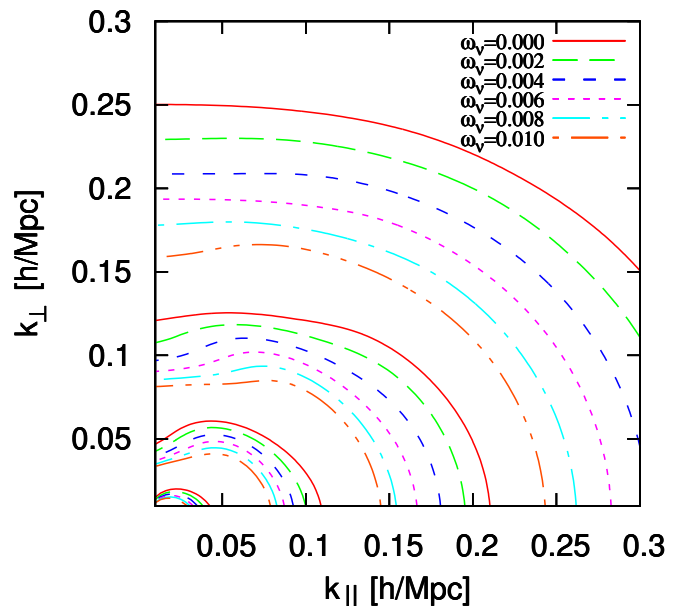


FIG. 11: Logarithmic contours of the redshift-space power spectrum $P_s(k_{\parallel}, k_{\perp})$ at $z = 1$. The neutrino density parameter $\omega_{\nu} = \Omega_{\nu,0} h^2$ is varied from its Λ CDM value of zero, with the early-time (large-scale) power spectrum normalization equal for all ω_{ν} , and all other parameters fixed at their Λ CDM values. This normalization convention corresponds to σ_8 of 0.8, 0.754, 0.705, 0.660, 0.618, and 0.580 for ω_{ν} of 0, 0.002, 0.004, 0.006, 0.008, and 0.01, respectively.

extent than those in Fig. 10. Figure 12 presents this effect in a different way by showing the fractional changes in the quadrupole caused by varying ω_{ν} , w_0 , and w_a relative to their massless-neutrino Λ CDM values. This dependence arises from the small-scale suppression of growth by massive neutrinos, which enters the linear redshift-space power spectrum through a scale-dependence in $f(z, k) = -\partial \log D(z, k) / \partial \log(1+z)$, a suppression of non-linear corrections, and a greater linear-theory velocity dispersion. Thus an analysis of redshift-space distortions provides one more method for distinguishing between the cosmological effects of massive neutrinos and evolving dark energy.

IV. COMPARISON WITH SIMULATIONS

A. N-body simulations with HACC

In order to test the accuracy of our perturbative calculation, we have run a suite of N-body cosmological simulations using the Hardware/Hybrid-Accelerated Cosmology Code (HACC), described in Ref. [49]. For each model in Table I we ran a high-resolution TreePM simulation with 3200^3 particles and a box size of $(2.1 \text{ Gpc})^3$. Additionally, we averaged the results of 16 PM runs, each with 512^3 particles and a box size of $(1.3 \text{ Gpc})^3$, in order to reduce the simulation error at quasi-linear scales

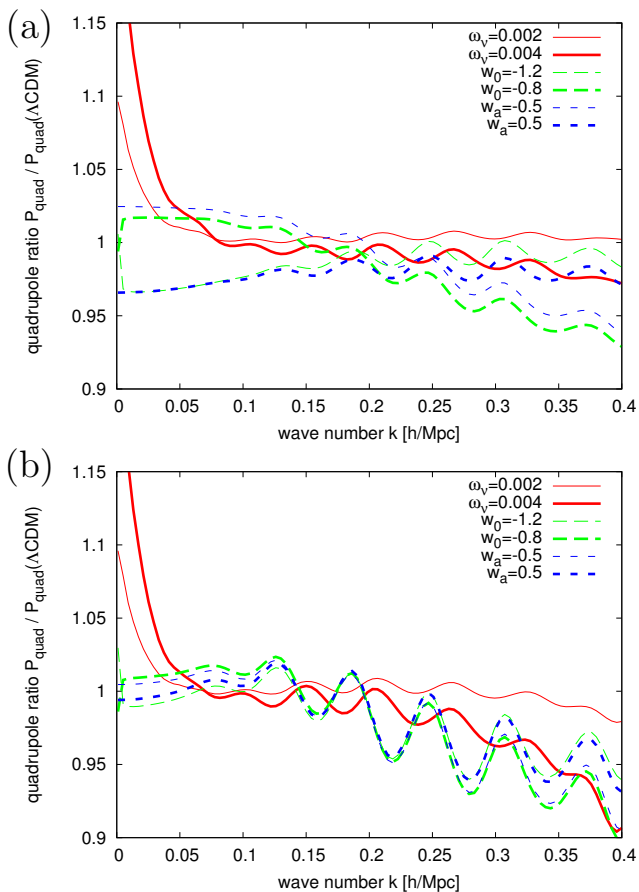


FIG. 12: Sensitivity of the quadrupole to changes in ω_ν , w_0 , and w_a relative to their values in model Λ CDM at (a) $z = 1$ and (b) $z = 0$. Shown for each model is the ratio of its quadrupole to that of Λ CDM, assuming linear theory for σ_ν .

$k \sim 0.1 h/\text{Mpc}$. Redshift-space power spectra $P_s(k_\parallel, k_\perp)$ were computed in the distant-observer approximation. Assuming the observer to be located far from the simulation volume along one of the three coordinate axes, we used each particle's line-of-sight velocity to shift its position from real space to redshift space. Fourier transformation of this shifted particle distribution yields a measurement of P_s , which can then be averaged over multiple simulation runs and all three lines of sight.

Our simulations treat massive neutrinos using the linear approximation of Refs. [47, 48], as described in Sec. II B. Particles in the simulation represent only the baryons and cold dark matter. After their non-linear power spectrum has been computed, the linear neutrino power (calculated using Boltzmann integrators such as CAMB and CMBFAST [57–59, 67]) is added using Eq. (18). This approximation was shown in Ref. [46] to agree well with perturbative results, with a discrepancy at large z and ω_ν that can approximately be corrected by including the scale-dependence of the linear growth factor. For an alternative approach to simulating massive neutrino cosmologies, see, for example, [61].

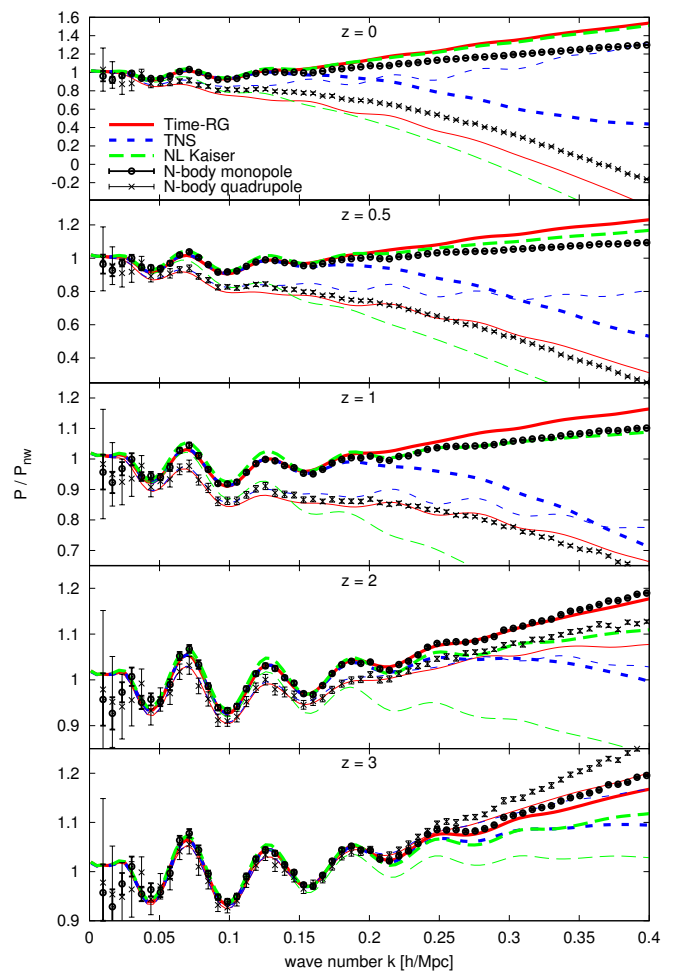


FIG. 13: Monopoles (thick lines) and quadrupoles (thin lines) of $P_s(k, \mu)$ computed using Time-RG, TNS [39], nonlinear Kaiser, and N-body methods, for the $m_\nu = 0$ model Λ CDM.

B. $m_\nu = 0$ Λ CDM and σ_ν fitting

Perturbative calculations for the massless-neutrino model Λ CDM are compared with N-body simulations in Figure 13. At each redshift, the velocity dispersion parameter σ_ν in the Lorentzian streaming function is fit to the N-body monopole and quadrupole by minimizing χ^2 . The N-body error in each k bin is the quadrature sum of the sample variance and the run-to-run standard deviation in the 16 simulation runs, divided by $\sqrt{16}$. Since errors in the perturbative calculations in the fully non-linear regime would bias the σ_ν fitting, resulting in a worse fit at low k , we restricted the fitting procedure to the range $k < k_{\text{max}} = 0.2 h/\text{Mpc}$. Even then, at $z = 0$, errors in the perturbative calculations appear to bias σ_ν . Time-RG in real space overestimates $P(k)$ at $k \sim 0.2 h/\text{Mpc}$, leading to an overestimate of σ_ν , hence an underestimate in the quadrupole. Closure theory at 1-loop, used in the TNS calculation, has the opposite

TABLE II: Wave number k [h/Mpc] below which each perturbation theory is accurate to the given accuracy level (Acc.) in the ΛCDM massless-neutrino model. “NL Kaiser” uses the Time-RG real-space power spectrum in the Kaiser RSD formula, Eq. (19).

z	Acc.	Time-RG		TNS [39]		NL Kaiser	
		$\ell = 0$	$\ell = 2$	$\ell = 0$	$\ell = 2$	$\ell = 0$	$\ell = 2$
0	1%	0.13	0.09	0.14	0.11	0.08	0.12
	2%	0.13	0.09	0.15	0.11	0.08	0.13
	5%	0.18	0.11	0.17	0.13	0.17	0.13
	10%	0.26	0.11	0.18	0.14	0.27	0.14
0.5	1%	0.15	0.11	0.17	0.15	0.11	0.07
	2%	0.19	0.11	0.17	0.15	0.12	0.07
	5%	0.21	0.29	0.19	0.15	0.32	0.15
	10%	0.33	0.33	0.23	0.20	1.17	0.19
1	1%	0.19	0.28	0.19	0.16	0.08	0.07
	2%	0.20	0.33	0.19	0.20	0.12	0.07
	5%	0.37	0.40	0.23	0.21	0.70	0.19
	10%	1.07	0.47	0.28	0.32	0.92	0.20
2	1%	0.36	0.24	0.21	0.28	0.21	0.19
	2%	0.43	0.30	0.23	0.29	0.26	0.19
	5%	0.56	0.43	0.29	0.34	0.34	0.20
	10%	0.72	0.54	0.34	0.41	0.49	0.25
3	1%	0.29	0.28	0.23	0.28	0.21	0.19
	2%	0.36	0.31	0.28	0.29	0.26	0.19
	5%	0.50	0.40	0.34	0.36	0.34	0.23
	10%	0.66	0.51	0.41	0.43	0.49	0.29

effect. For $z \gtrsim 1$, both perturbative calculations agree well with the simulation. The σ_v fitting procedure is discussed further in Appendix C, which shows that our results are insensitive to the value of k_{max} within the range $0.15 h/\text{Mpc} \leq k_{\text{max}} \leq 0.25 h/\text{Mpc}$.

Table II uses the data from Fig. 13 to list the maximum k up to which each perturbative calculation agrees with simulations to a given accuracy level. The results follow the broad patterns expected from Fig. 1: for percent-level accuracy at $z \lesssim 0.5$, the closure-theory-based approach of TNS is somewhat better than Time-RG, while for 5%-10% accuracy levels and at higher z , Time-RG is preferred. In particular, we note that Time-RG diverges from the N-body power spectra rather smoothly, with no model-dependent catastrophic errors which could bias data analyses or forecasts. Meanwhile, the non-linear Kaiser model, which uses the Time-RG non-linear power spectrum instead of the linear one in Eq. (19), fails to match accurately the N-body quadrupole even at $z \sim 1$.

Similar patterns can be seen in Figure 14, which shows the two-dimensional power spectrum $P_s(k_{\parallel}, k_{\perp})$ for simulations, Time-RG, TNS, and the non-linear Kaiser model. The trends seen in Fig. 13 are evident here: Time-RG overestimates the monopole, particularly at $z = 0$; TNS underestimates the monopole; and the Kaiser model sub-

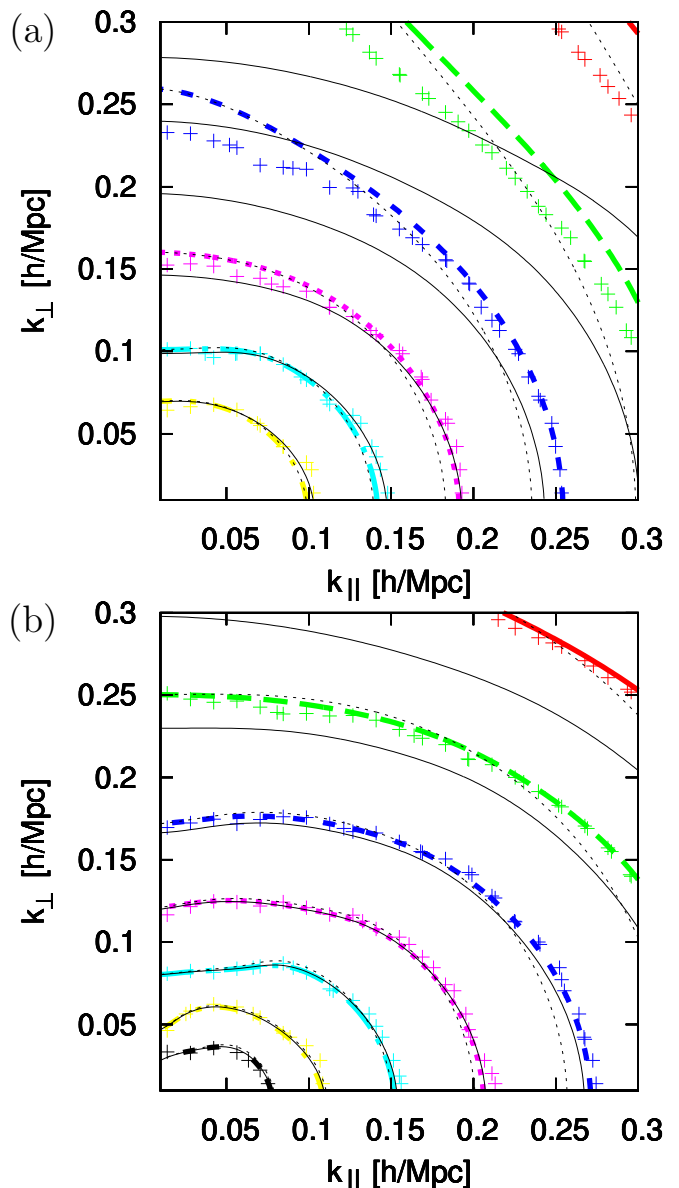


FIG. 14: Logarithmic contours of the redshift-space power spectrum $P_s(k_{\parallel}, k_{\perp})$ for the massless-neutrino model ΛCDM , at (a) $z = 0$; (b) $z = 1$. Points show N-body calculations, thick dashed (colored) lines show Time-RG, solid black lines show TNS, and thin dashed black lines show the non-linear Kaiser approximation.

stantially underestimates the quadrupole, even at $z = 1$.

C. Evolving dark energy and massive neutrinos

Finally, we apply our calculation to the last three models in Table I: an early dark energy, a massive-neutrino ΛCDM model, and a dark energy with $w_a = -1.11$ and massive neutrinos. Since next-generation galaxy surveys will go beyond the BOSS redshift [2] of $z = 0.57$ to $z \approx 1$, we focus here on $z = 1$ and 0. Evidently from Figure 15,

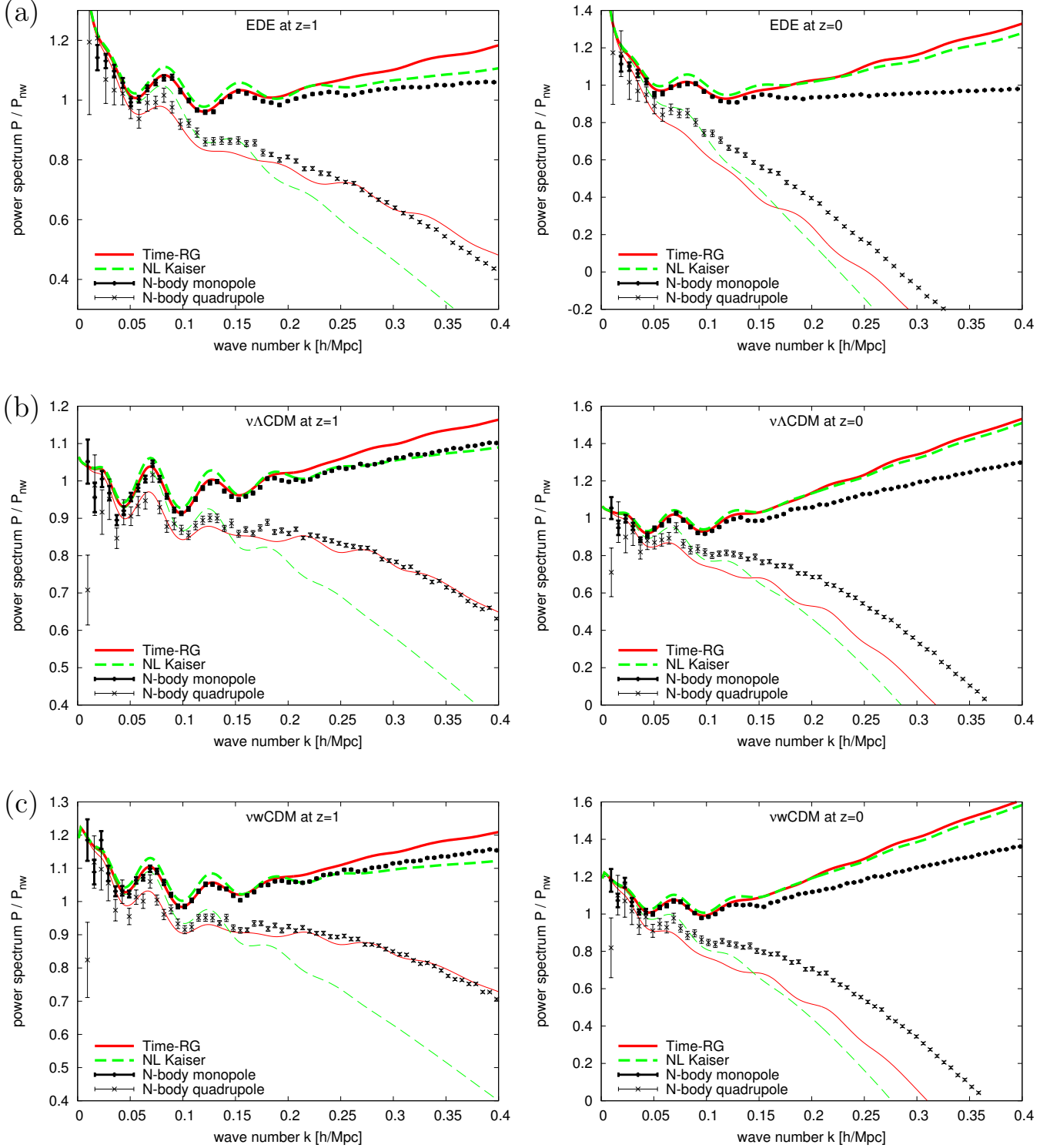


FIG. 15: Monopoles (thick lines) and quadrupoles (thin lines) of the redshift-space power spectra at (left) $z = 1$ and (right) $z = 0$ for (a) EDE, early dark energy with massless neutrinos; (b) $\nu\Lambda\text{CDM}$, with $\sum m_\nu = 0.094$ eV; (c) $\nu w\text{CDM}$, a rapidly-evolving dark energy with $\sum m_\nu = 0.29$ eV. In each case, points represent N-body calculations, solid (red) lines show the Time-RG calculation, and dashed (green) lines show the non-linear Kaiser model.

TABLE III: Wave number k [h/Mpc] below which each perturbation theory is accurate to the given accuracy level (Acc.) for the models in Table I. “NL Kaiser” uses the Time-RG real-space power spectrum in the Kaiser RSD formula, Eq. (19).

z	Acc.	EDE				$\nu\Lambda\text{CDM}$				νwCDM			
		Time-RG		NL Kaiser		Time-RG		NL Kaiser		Time-RG		NL Kaiser	
		$\ell = 0$	$\ell = 2$	$\ell = 0$	$\ell = 2$	$\ell = 0$	$\ell = 2$	$\ell = 0$	$\ell = 2$	$\ell = 0$	$\ell = 2$	$\ell = 0$	$\ell = 2$
0	1%	0.11	0.06	0.04	0.10	0.11	0.06	0.05	0.12	0.12	0.06	0.06	0.11
	2%	0.12	0.07	0.04	0.10	0.13	0.06	0.06	0.12	0.13	0.06	0.06	0.11
	5%	0.16	0.07	0.12	0.10	0.16	0.06	0.16	0.13	0.15	0.08	0.15	0.11
	10%	0.20	0.07	0.21	0.11	0.25	0.11	0.27	0.14	0.25	0.11	0.26	0.13
0.5	1%	0.16	0.10	0.07	0.15	0.13	0.06	0.05	0.06	0.14	0.08	0.04	0.04
	2%	0.17	0.10	0.07	0.15	0.15	0.11	0.05	0.06	0.15	0.08	0.04	0.06
	5%	0.22	0.10	0.22	0.16	0.21	0.12	0.32	0.14	0.21	0.11	0.35	0.06
	10%	0.25	0.15	0.33	0.16	0.34	0.49	1.17	0.17	0.33	0.39	1.12	0.16
1	1%	0.18	0.10	0.07	0.09	0.19	0.17	0.06	0.06	0.15	0.13	0.06	0.06
	2%	0.18	0.10	0.07	0.09	0.19	0.17	0.06	0.06	0.21	0.17	0.06	0.06
	5%	0.25	0.16	0.47	0.18	0.36	0.45	0.70	0.15	0.89	0.46	0.52	0.16
	10%	0.38	0.39	1.20	0.19	1.07	0.52	0.92	0.20	1.00	0.52	0.75	0.19
2	1%	0.25	0.41	0.12	0.09	0.45	0.30	0.06	0.08	0.37	0.25	0.12	0.08
	2%	0.25	0.55	0.36	0.18	0.49	0.35	0.26	0.08	0.44	0.31	0.27	0.13
	5%	1.06	0.83	0.53	0.19	0.62	0.47	0.36	0.20	0.54	0.37	0.35	0.21
	10%	1.13	1.10	0.85	0.25	0.79	0.62	0.53	0.26	0.69	0.54	0.49	0.26
3	1%	0.62	0.39	0.26	0.19	0.36	0.34	0.26	0.20	0.37	0.37	0.23	0.13
	2%	0.69	0.44	0.33	0.19	0.45	0.38	0.26	0.20	0.44	0.37	0.28	0.21
	5%	0.86	0.58	0.44	0.25	0.60	0.51	0.38	0.25	0.58	0.52	0.40	0.26
	10%	1.05	0.75	0.65	0.31	0.77	0.65	0.55	0.32	0.74	0.65	0.57	0.33

the Time-RG RSD calculation presented here agrees well with N-body calculations of the monopole, quadrupole, and two-dimensional redshift-space power spectrum for a wide range of models at $z = 1$. By contrast, the Kaiser RSD model, Eq. (19) applied to the non-linear real-space power spectrum, substantially underpredicts the quadrupole at quasi-linear scales. At $z = 0$, neither perturbative calculation is accurate beyond $k \approx 0.1 h/\text{Mpc}$ for any of the models. Table III lists the accuracy of both perturbative methods for all three models over the redshift range $0 \leq z \leq 3$.

V. CONCLUSIONS

Cosmological surveys over the next decade will measure the sum of neutrino masses, and should either detect or decisively exclude order-unity variations in the dark energy equation of state. Observations are made in redshift space, with the redshift dependent on the line-of-sight velocity of an object as well as its distance. Since peculiar velocities are sourced by overdensities, redshift-space distortions provide additional information about the scale-dependent growth of large-scale structure. Perturbative techniques for calculating the redshift-space power spectrum in models with scale-independent growth were reviewed in Ref. [40], with the method by Taruya,

Nishimichi, and Saito [39] (TNS) proving the most effective.

In this article we have extended the TNS approach to models with scale-dependent growth using the Time-RG perturbation theory, in which higher-order contributions to the power spectrum are described in terms of the bispectrum. We have decomposed the higher-order corrections found by TNS into integrals $Q_{abc}^{(\ell)}(k)$ over the bispectrum. Using the Time-RG framework, we have derived the evolution equations for the $Q_{abc}^{(\ell)}$ and computed the redshift-space power spectrum in models with massive neutrinos as well as rapidly-evolving dark energy. Finally, we have confirmed the accuracy of our calculations by comparing them to N-body simulations conducted using the HACC code. We compare our results to TNS and simulations in Figures 13 and 14 as well as in Table II. Figure 15 and Table III show that our results agree closely with N-body simulations for a wide range of models with massive neutrinos and rapidly-evolving dark energy equations of state.

Our work is applicable in a variety of ways. Since our results are accurate at the 10% level over a fairly large range of wave numbers, particularly for $z \gtrsim 1$, they can be used to forecast constraints from large-scale structure surveys. Forecasts based upon linear perturbation theory are truncated at $k \sim 0.1 h/\text{Mpc}$, since linear theory at

smaller scales overestimates the amount of information available from the BAO peak [3]. Accuracy can be improved by building an emulator combining our perturbative calculation at large scales with interpolated N-body power spectra at small scales [68, 69]. Finally, perturbative techniques allowing for scale-dependent growth are applicable to modified gravity as well as to massive neutrinos.

Appendix A: Evolution of P_B in Time-RG

Rather than computing the full functional dependence of the bispectrum $B(k, q, p)$ on three different wave numbers, we may decompose $P_B(k, \mu)$ into a set of k -dependent bispectrum integrals whose time-evolution may be computed within the Time-RG framework. Expanding the expression (25), we have

$$\begin{aligned} \frac{P_B}{k\mu} = & - \int \frac{d^3q}{(2\pi)^3} \frac{\mu_{\vec{q}}}{q} \left[B_{\delta\theta\delta}(k, q, p_+) \right. \\ & - \mu^2 B_{\theta\theta\delta}(k, q, p_+) - \mu_{\vec{p}_+}^2 B_{\delta\theta\theta}(k, q, p_+) \\ & \left. + \mu^2 \mu_{\vec{p}_+}^2 B_{\theta\theta\theta}(k, q, p_+) \right] - [\vec{p}_+ \leftrightarrow \vec{p}_-] \quad (\text{A1}) \end{aligned}$$

where $\vec{p}_\pm = \vec{k} \pm \vec{q}$ implies $p_\pm^2 \mu_{\vec{p}_\pm}^2 = k^2 \mu^2 + q^2 \mu_{\vec{q}}^2 \pm 2kq\mu\mu_{\vec{q}}$. The three-dimensional integral over \vec{q} can be evaluated as the integral over the magnitude q , the angle α between \vec{q} and \vec{k} , and the angle β of $\vec{q} - (\hat{q} \cdot \hat{k})\vec{k}$ in the plane perpendicular to \vec{k} . Since $B_{abc}(\vec{k}_1, \vec{k}_2, \vec{k}_3)$ is invariant under rotation in \vec{k}_i -space, the only β -dependent quantities in the integral are factors of $\mu_{\vec{q}}$ raised to integer powers; thus, the integral over β can be evaluated trivially.

Define the quantities

$$Q_{abc}^{(\ell)}(k) = \int \frac{q^2 dq \sin(\alpha) d\alpha}{(2\pi)^3} \frac{k}{p_+^2} \left(\frac{q}{k}\right)^{\sigma_\ell} \mathcal{P}_{|\ell|}(\cos \alpha) \times B_{abc}(k, q, p_+) + (-1)^\ell [\vec{p}_+ \leftrightarrow \vec{p}_-] \quad (\text{A2})$$

$$\sigma_\ell = \begin{cases} \text{sign}(\ell) & \text{if } \ell \text{ is odd} \\ 0 & \text{if } \ell \text{ is even} \end{cases} \quad (\text{A3})$$

for $\ell = -1, 0, 1, 2$, and 3 , where the \mathcal{P} are Legendre polynomials. Then

$$\begin{aligned} \frac{P_{B,2}}{\pi k} = & -2Q_{\delta\theta\delta}^{(-1)} - 2Q_{\delta\theta\delta}^{(1)} - \frac{8}{3}Q_{\delta\theta\delta}^{(2)} - \frac{4}{3}Q_{\delta\theta\delta}^{(0)} \\ & + \frac{4}{3}Q_{\delta\theta\theta}^{(2)} - \frac{4}{3}Q_{\delta\theta\theta}^{(0)} + \frac{6}{5}Q_{\delta\theta\theta}^{(3)} - \frac{6}{5}Q_{\delta\theta\theta}^{(1)} \quad (\text{A4}) \end{aligned}$$

$$\begin{aligned} \frac{P_{B,4}}{\pi k} = & -2Q_{\theta\theta\delta}^{(-1)} - 2Q_{\theta\theta\delta}^{(1)} - \frac{8}{3}Q_{\theta\theta\delta}^{(2)} - \frac{4}{3}Q_{\theta\theta\delta}^{(0)} \\ & - 2Q_{\delta\theta\theta}^{(-1)} - 4Q_{\delta\theta\theta}^{(2)} - 2Q_{\delta\theta\theta}^{(3)} + \frac{4}{3}Q_{\theta\theta\theta}^{(2)} \\ & - \frac{4}{3}Q_{\theta\theta\theta}^{(0)} + \frac{6}{5}Q_{\theta\theta\theta}^{(3)} - \frac{6}{5}Q_{\theta\theta\theta}^{(1)} \quad (\text{A5}) \end{aligned}$$

$$\frac{P_{B,6}}{\pi k} = -2Q_{\theta\theta\theta}^{(-1)} - 4Q_{\theta\theta\theta}^{(2)} - 2Q_{\theta\theta\theta}^{(3)} \quad (\text{A6})$$

where the $P_{B,j}$ and $Q_{abc}^{(\ell)}$ are understood to depend on k .

Next, we study the evolution of the $Q_{abc}^{(\ell)}$ in Time-RG. Since the evolution of the $B_{abc}(k, q, p)$ only depends on the other components of $B_{abc}(k, q, p)$, the evolution of the $Q_{abc}^{(\ell)}$ for fixed ℓ will only depend on the other components of $Q_{abc}^{(\ell)}$. We can easily multiply the bispectrum evolution equation (11) by $(k/p_\pm^2)(q/k)^{\sigma_\ell} \mathcal{P}_{|\ell|}(\cos \alpha)$, integrate over d^3q , and pull the time derivative outside of the integral. Therefore,

$$\partial_\eta Q_{abc}^{(\ell)} = -\Omega_{ad}Q_{dbc}^{(\ell)} - \Omega_{bd}Q_{adc}^{(\ell)} - \Omega_{cd}Q_{abd}^{(\ell)} + 2e^\eta R_{abc}^{(\ell)} \quad (\text{A7})$$

$$\begin{aligned} R_{abc}^{(\ell)}(k) = & \int \frac{q^2 dq \sin \alpha d\alpha}{(2\pi)^3} \frac{k}{p_+^2} \left(\frac{q}{k}\right)^{\sigma_\ell} \mathcal{P}_{|\ell|}(\cos \alpha) \\ & \times \left[\gamma_{ade}(k, q, p_+) P_{ab}(q) P_{ec}(p_+) \right. \\ & + \gamma_{bde}(q, p_+, k) P_{dc}(p_+) P_{ea}(k) \\ & \left. + \gamma_{cde}(p_+, k, q) P_{da}(k) P_{eb}(q) \right] + (-1)^\ell [\vec{p}_+ \leftrightarrow \vec{p}_-] \quad (\text{A8}) \end{aligned}$$

where the $Q_{abc}^{(\ell)}$ and $R_{abc}^{(\ell)}$ at each η depend only on k .

Appendix B: Computation of P_T

Beginning with Eq. (26), we find P_T by integrating over the angle β of \vec{q} in the plane perpendicular to \vec{k} . Once again defining α as the angle between \vec{k} and \vec{q} , and defining $\tau_{ab} = P_{a,\theta}(q)P_{b,\theta}(p_-)$,

$$\frac{P_{T,j}}{\pi k^2} = \int \frac{q^2 dq s_\alpha d\alpha}{(2\pi)^3 p_-^2} \sum_{ab} S_{ab,j} \tau_{ab} \quad \text{for } j = 2, 4, 6, 8 \quad (\text{B1})$$

where the $S_{ab,j}$ are given by:

$$S_{\delta\delta,2} = -s_\alpha^2 \quad (\text{B2})$$

$$S_{\delta\theta,2} = -3s_\alpha^4 q^2 / (4p_-^2) \quad (\text{B3})$$

$$S_{\theta\delta,2} = -3s_\alpha^6 / 4 \quad (\text{B4})$$

$$S_{\theta\theta,2} = -5s_\alpha^6 / 8 \quad (\text{B5})$$

$$S_{\delta\delta,4} = 2c_\alpha k/q + s_\alpha^2 - 2c_\alpha^2 \quad (\text{B6})$$

$$S_{\delta\theta,4} = -3s_\alpha^2 \frac{k^2}{p_-^2} + 9c_\alpha s_\alpha^2 \frac{kq}{p_-^2} + s_\alpha^2 (s_\alpha^2 - 4c_\alpha^2) \frac{3q^2}{2p_-^2} \quad (\text{B7})$$

$$S_{\theta\delta,4} = 3c_\alpha s_\alpha^2 k/q + 3s_\alpha^2 (s_\alpha^2 - 4c_\alpha^2) / 2 \quad (\text{B8})$$

$$S_{\theta\theta,4} = -s_\alpha^4 \frac{9k^2}{4p_-^2} + c_\alpha^2 s_\alpha^4 \frac{45kq}{4p_-^2} + s_\alpha^4 (s_\alpha^2 - 6c_\alpha^2) \frac{15q^2}{8p_-^2} \quad (\text{B9})$$

$$\begin{aligned} S_{\delta\theta,6} = & c_\alpha^3 / qp_-^2 + 3(s_\alpha^2 - 2c_\alpha^2) kq / p_-^2 \\ & + 6(c_\alpha^2 s_\alpha^2 - c_\alpha^4 / 3 - s_\alpha^4 / 8) 6q^2 / p_-^2 \quad (\text{B10}) \end{aligned}$$

$$S_{\theta\delta,6} = (2c_\alpha^2 - 3s_\alpha^2) k/q + 6(c_\alpha^2 s_\alpha^2 - c_\alpha^4 / 3 - s_\alpha^4 / 8) \quad (\text{B11})$$

$$\begin{aligned} S_{\theta\theta,6} = & 3c_\alpha s_\alpha^2 k^3 / (qp_-^2) + 9s_\alpha^2 (s_\alpha^2 - 4c_\alpha^2) k^2 / (4p_-^2) \\ & + 30(c_\alpha^3 s_\alpha^2 - c_\alpha s_\alpha^4 / 4) kq / p_-^2 \\ & + 45s_\alpha^2 (c_\alpha^2 s_\alpha^2 - 2c_\alpha^4 / 3 - s_\alpha^4 / 12) q^2 / (2p_-^2) \quad (\text{B12}) \end{aligned}$$

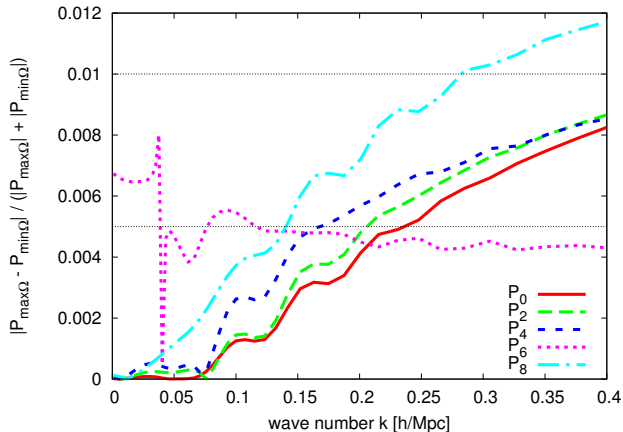


FIG. 16: Error associated with neglecting the k -dependence of Ω_{10} , Eq. (6), in the non-linear Time-RG corrections Eqs. (14,A7). Differences between power spectra computed with the maximum and minimum values of Ω_{10} are shown at $z = 0$ for a model with $\omega_\nu = 0.01$, corresponding to $\sum m_\nu = 0.94$ eV.

$$\begin{aligned}
 S_{\theta\theta,8} = & (2c_\alpha^3 - 3c_\alpha s_\alpha^2) \frac{k^3}{qp^2} + 18(c_\alpha^2 s_\alpha^2 - \frac{1}{3}c_\alpha^4 - \frac{1}{8}s_\alpha^4) \frac{k^2}{p_-^2} \\
 & + 6(c_\alpha^6 - 5c_\alpha^3 s_\alpha^2 + \frac{15}{8}c_\alpha s_\alpha^4) \frac{kq}{p_-^2} \\
 & - (2c_\alpha^6 - 15c_\alpha^4 s_\alpha^2 + \frac{45}{4}c_\alpha^2 s_\alpha^4 - \frac{5}{8}s_\alpha^6) \frac{q^2}{p_-^2} \quad (\text{B13})
 \end{aligned}$$

We have used the shorthand notation $s_\alpha = \sin(\alpha)$ and $c_\alpha = \cos(\alpha)$. All components of $S_{ab,j}$ not listed above are zero.

Appendix C: Error bounds and σ_v fits

1. Scale-dependence of Ω

In the general multi-species case as well as in the linear neutrino approximation of Sec. II B, the linear evolution matrix Ω is scale-dependent. In particular, Eq. (6) shows that the fractional change in Ω_{10} is of order f_ν in massive neutrino models. This scale-dependence has been neglected in real-space and redshift-space Time-RG, Eqs. (14,A7), in which Ω has been pulled outside the integrals over wave number. Here we estimate the error associated with this approximation and show that it is small enough to be negligible even for neutrino masses several times current bounds.

In order to place an upper bound on this k -dependent Ω error, we study a model similar to $\nu\Lambda\text{CDM}$ but with ten times the neutrino content, $\omega_\nu = 0.01$, corresponding to $\sum m_\nu = 0.94$ eV. The function $\Omega_{10}(z, k)$ drops from a maximum value at large scales, where neutrinos cluster like cold matter, to a small-scale value that is smaller by a fraction $\approx f_\nu/(1 - f_\nu)$. Moreover, we expect the error to be smaller at higher z , since it only affects non-linear correction terms, which grow with time.

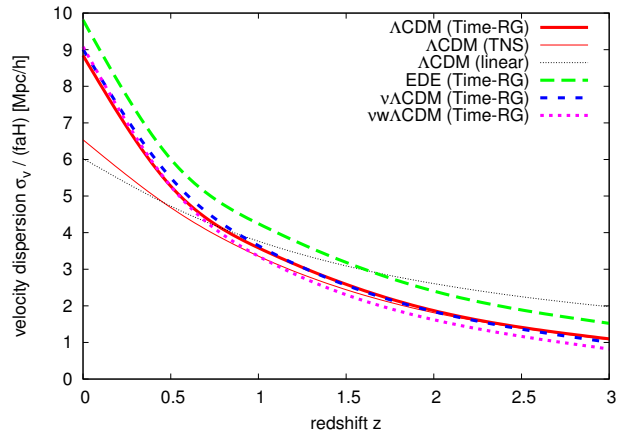


FIG. 17: Best-fit velocity dispersion σ_v for the models in Table I, fitting to a suite of 15 Particle-Mesh N-body simulations at scales $k \leq k_{\text{max}} = 0.2$ h/Mpc .

We estimate the k -dependent Ω error by computing power spectra using either the maximum or the minimum values of Ω_{10} in Eqs. (14,A7). Our estimate, half the difference between the two, is shown in Fig. 16 for the power spectrum components $P_j(k)$ defined in Eq. 29. For the dominant contributors to the redshift-space power spectrum, P_0 , P_2 , and P_4 , the error is less than 0.5% for $k \leq 0.15$ h/Mpc and less than 0.9% for $k \leq 0.4$ h/Mpc . Errors in the smaller terms P_6 and P_8 are less than 1% for $k \leq 0.25$ h/Mpc . At higher z , and for more realistic f_ν , we expect these errors to be several times smaller, meaning that they are negligible compared with the errors listed in Tables II and III.

2. Best-fit σ_v

Our results in Tables II and III are based on fitting the velocity dispersion σ_v in the Lorentzian streaming function $F_{\text{fog}}(f\sigma_v k\mu)$ to the N-body simulations over the range $k \leq k_{\text{max}} = 0.2$ h/Mpc . The resulting velocity dispersions are shown in Fig. 17 for the models in Table I. Velocity dispersions for models ΛCDM , $\nu\Lambda\text{CDM}$, and $\nu w\Lambda\text{CDM}$ are similar, while the early dark energy model EDE, which enhances structure growth, has a larger velocity dispersion. Also shown, for ΛCDM , are the velocity dispersion in the TNS calculation and that of linear theory, Eq. (22). For ΛCDM , both non-linear calculations find σ_v below linear theory at high z and above linear theory at low z . The best-fit σ_v values appear to be biased by perturbation theory errors at low z . Time-RG, which overpredicts late-time small-scale power, has a higher σ_v than TNS, which underpredicts it.

TABLE IV: Sensitivity to k_{\max} . Wave numbers k [h/Mpc] below which Time-RG perturbation theory is accurate to the given accuracy level (Acc.) for model $\nu\Lambda\text{CDM}$ are shown. In each case, the velocity dispersion σ_v in the streaming function $F_{\text{fog}}(f\sigma_v k\mu)$ was fit to the N-body power spectrum over the range $k \leq k_{\max}$. For comparison, Tables II and III used $k_{\max} = 0.2 h/\text{Mpc}$.

z	Acc.	$\frac{k_{\max}}{h/\text{Mpc}} = 0.1$		$\frac{k_{\max}}{h/\text{Mpc}} = 0.15$		$\frac{k_{\max}}{h/\text{Mpc}} = 0.25$	
		$\ell = 0$	$\ell = 2$	$\ell = 0$	$\ell = 2$	$\ell = 0$	$\ell = 2$
0	1%	0.09	0.06	0.11	0.06	0.13	0.06
	2%	0.11	0.06	0.13	0.06	0.13	0.06
	5%	0.14	0.11	0.15	0.11	0.19	0.06
	10%	0.21	0.17	0.21	0.11	0.27	0.11
0.5	1%	0.13	0.11	0.13	0.11	0.14	0.06
	2%	0.13	0.12	0.13	0.11	0.19	0.06
	5%	0.19	0.17	0.21	0.17	0.26	0.11
	10%	0.30	0.36	0.32	0.40	0.42	0.17
1	1%	0.16	0.17	0.17	0.17	0.19	0.14
	2%	0.19	0.17	0.19	0.17	0.21	0.17
	5%	0.32	0.36	0.32	0.44	0.96	0.17
	10%	1.09	0.45	1.07	0.49	1.04	0.59
2	1%	0.19	0.19	0.41	0.17	0.41	0.29
	2%	0.28	0.21	0.49	0.30	0.49	0.30
	5%	0.78	0.86	0.60	0.38	0.61	0.38
	10%	0.96	0.99	0.77	0.58	0.77	0.59
3	1%	0.19	0.18	0.36	0.34	0.35	0.34
	2%	0.28	0.19	0.45	0.38	0.45	0.35
	5%	1.08	0.28	0.58	0.49	0.58	0.49
	10%	1.14	0.53	0.76	0.64	0.76	0.62

3. Sensitivity to k_{\max}

In the quasi-linear regime, errors in perturbation theory increase with increasing k , while uncertainties in

N-body simulations and actual data decrease due to a greater number of modes. Thus one might worry that our σ_v fitting procedure is dominated by wave numbers near k_{\max} , which may be at the edge of the regime of validity of perturbation theory. Table IV tests the sensitivity of our redshift-space Time-RG perturbative calculation to k_{\max} for model $\nu\Lambda\text{CDM}$. The table shows wave numbers up to which perturbation theory is accurate for several accuracy thresholds, for $k_{\max} = 0.1 h/\text{Mpc}$, $0.15 h/\text{Mpc}$, and $0.25 h/\text{Mpc}$. Comparison to Table III shows that $k_{\max} = 0.15 h/\text{Mpc}$, $0.2 h/\text{Mpc}$, and $0.25 h/\text{Mpc}$ are similar. At the 1 – 2% accuracy levels and at $z \geq 2$, $k_{\max} = 0.1 h/\text{Mpc}$ leads to a significantly worse fit. This is not surprising, since the N-body error bars in Fig. 15 (b) are large for $k < 0.1 h/\text{Mpc}$, and since not much non-linear information is available at such large scales. We conclude that our results are stable over the range $0.15 h/\text{Mpc} \leq k_{\max} \leq 0.25 h/\text{Mpc}$.

Acknowledgments

We are grateful to D. Chung, E. Jennings, T. Okumura, and M. Takada for insightful discussions. The authors were supported by the U.S. Department of Energy, Basic Energy Sciences, Office of Science, under contract No. DE-AC02-06CH11357. This research used resources of the ALCF, which is supported by DOE/SC under contract DE-AC02-06CH11357 and resources of the OLCF, which is supported by DOE/SC under contract DE-AC05-00OR22725.

The submitted manuscript has been created by UChicago Argonne, LLC, Operator of Argonne National Laboratory (“Argonne”). Argonne, a U.S. Department of Energy Office of Science laboratory, is operated under Contract No. DE-AC02-06CH11357. The U.S. Government retains for itself, and others acting on its behalf, a paid-up nonexclusive, irrevocable worldwide license in said article to reproduce, prepare derivative works, distribute copies to the public, and perform publicly and display publicly, by or on behalf of the Government.

-
- [1] P. A. R. Ade et al. 2015. e-Print arXiv:1502.01589.
[2] L. Anderson et al. *Mon. Not. Roy. Astron. Soc.*, 441:24, 2014.
[3] A. Font-Ribera, P. McDonald, N. Mostek, B. A. Reid, H.-J. Seo, et al. *JCAP*, 1405:023, 2014.
[4] D. Schlegel, M. White, and D. Eisenstein. 2009. e-Print: arXiv:0902.4680.
[5] M. Levi et al. 2013. e-Print: arXiv:1308.0847.
[6] T. Abbott et al. 2005. e-Print: astro-ph/0510346.
[7] P. A. Abell et al. 2009. e-Print: arXiv:0912.0201.
[8] A. Refregier et al. 2010. e-Print: arXiv:1001.0061.
[9] T. Basse, O. Eggers Bjaelde, J. Hamann, S. Hannestad, and Y. Y. Y. Wong. *JCAP*, 1405:021, 2014.
[10] A. Vikhlinin et al. *Astrophys. J.*, 692:1060, 2009.
[11] A. Conley. *Astrophys. J. Supp.*, 192:1, 2011.
[12] N. Suzuki et al. *Astrophys. J.*, 746:85, 2012.
[13] M. Kilbinger et al. *Mon. Not. R. Astron. Soc.*, 430:2200, 2013.
[14] G. Hinshaw et al. *Astrophys. J. Supp. Ser.*, 208:19, 2013.
[15] Z. Hou et al. *Astrophys. J.*, 782:74, 2014.
[16] E. Calabrese et al. *Phys. Rev. D*, 87:103012, 2013.
[17] P. A. R. Ade et al. 2013. e-Print arXiv:1303.5076.
[18] S. Weinberg. *Rev. Mod. Phys.*, 61:1, 1989.
[19] R. Bousoo and J. Polchinski. *JHEP*, 0006:006, 2000.
[20] *Found. Phys.*, 36:613, 2006.
[21] R. R. Caldwell and M. Kamionkowski. *Ann. Rev. Nucl. Part. Sci.*, 59:397, 2009.
[22] J. Martin. *Comp. Rend. Phys.*, 13:566, 2012.
[23] P. A. R. Ade et al. 2015. e-Print arXiv:1502.01590.
[24] P. Binetruy. *Phys. Rev. D*, 60:063502, 1999.
[25] I. Zlatev, L. Wang, and P. J. Steinhardt. *Phys. Rev. Lett.*, 82:896, 1999.

- [26] P. J. Steinhardt, L. Wang, and I. Zlatev. *Phys. Rev. D*, 59:123504, 1999.
- [27] C. Armendariz-Picon, V. F. Mukhanov, and P. J. Steinhardt. *Phys. Rev. Lett.*, 85:4438, 2000.
- [28] T. Barreiro, E. J. Copeland, and N. J. Nunes. *Phys. Rev. D*, 61:127301, 2000.
- [29] A. Upadhye, M. Ishak, and P. J. Steinhardt. *Phys. Rev. D*, 72:063501, 2005. e-Print: arXiv:astro-ph/0411803.
- [30] J. C. Bueno Sanchez and K. Dimopoulos. *Phys. Lett. B*, 642:294, 2006.
- [31] U. Alam. *Astrophys. J.*, 714:1460, 2010.
- [32] U. Alam, Z. Lukić, and S. Bhattacharya. *Astrophys. J.*, 727:87, 2011.
- [33] M. Betoule et al. *Astron. Astrophys.*, 552:124, 2013.
- [34] F. Beutler et al. *Mon. Not. Roy. Astron. Soc.*, 443:1065, 2014.
- [35] L. Samushia et al. *Mon. Not. Roy. Astron. Soc.*, 439:3504, 2014.
- [36] C. Heymans et al. *Mon. Not. Roy. Astron. Soc.*, 432:2433, 2013.
- [37] N. Kaiser. *Mon. Not. R. Astron. Soc.*, 227:1, 1987.
- [38] R. Scoccimarro. *Phys. Rev. D*, 70:083007, 2004.
- [39] A. Taruya, T. Nishimichi, and S. Saito. *Phys. Rev. D*, 82:063522, 2010. e-Print: arXiv:1006.0699.
- [40] J. Kwan, G. F. Lewis, and E. V. Linder. *Astrophys. J.*, 748:78, 2012.
- [41] M. Pietroni. *JCAP*, 10:036, 2008.
- [42] J. Lesgourgues, S. Matarrese, M. Pietroni, and A. Riotto. *JCAP*, 0906:017, 2009.
- [43] S. Anselmi, G. Ballesteros, and M. Pietroni. *JCAP*, 11:014, 2011.
- [44] J. Carlson, M. White, and N. Padmanabhan. *Phys. Rev. D*, 80:043531, 2009.
- [45] B. Audren and J. Lesgourgues. *JCAP*, 10:037, 2011.
- [46] A. Upadhye, R. Biswas, A. Pope, K. Heitmann, S. Habib, H. Finkel, and N. Frontiere. *Phys. Rev. D*, 89:103515, 2014.
- [47] S. Saito, M. Takada, and A. Taruya. *Phys. Rev. Lett.*, 100:191301, 2008.
- [48] S. Agarwal and H. A. Feldman. *Mon. Not. R. Astron. Soc.*, 410:1647, 2011.
- [49] S. Habib et al. *New Astron. (in press)*, 2014. e-Print arXiv:1410.2805.
- [50] M. Wyman, D. H. Rudd, R. A. Vanderveld, and W. Hu. *Phys. Rev. Lett.*, 112:051302, 2014.
- [51] D. Blas, M. Garny, T. Konstandin, and J. Lesgourgues. *JCAP*, 1411:039, 2014.
- [52] D. J. Eisenstein and W. Hu. *Astrophys. J.*, 496:605, 1998.
- [53] A. Taryua and T. Hiramatsu. *Astrophys. J.*, 674:617, 2008.
- [54] T. Hiramatsu and A. Taruya. *Phys. Rev. D*, 79:103526, 2009.
- [55] A. Taruya, T. Nishimichi, S. Saito, and T. Hiramatsu. *Phys. Rev. D*, 80:123503, 2009.
- [56] G. Juergens and M. Bartelmann. 2012. e-Print: arXiv:1204.6524.
- [57] A. Lewis, A. Challinor, and A. Lasenby. *Astrophys. J.*, 538:473, 2000.
- [58] U. Seljak and M. Zaldarriaga. *Ap. J.*, 469:437, 1996.
- [59] M. Zaldarriaga, U. Seljak, and E. Bertschinger. *Ap. J.*, 494:491, 1998.
- [60] F. Fühler and Y. Y. Y. Wong. *JCAP*, 1503:046, 2015.
- [61] E. Castorina, C. Carbone, J. Bel, E. Sefusatti, and K. Dolag. *JCAP*, 1507:043, 2015.
- [62] J. C. Jackson. *Mon. Not. Roy. Astron. Soc.*, 156:1P, 1972.
- [63] K. B. Fisher. *Astrophys. J.*, 448:494, 1995.
- [64] J. N. Fry. *Astrophys. J.*, 279:499, 1984.
- [65] M. Galassi et al. *GNU Scientific Library Reference Manual - Third Edition*. 2009.
- [66] T. Hahn. *Comput. Phys. Commun.*, 168:78, 2005.
- [67] M. Zaldarriaga and U. Seljak. *Ap. J. Supp.*, 129:431, 2000.
- [68] K. Heitmann, E. Lawrence, J. Kwan, S. Habib, and D. Higdon. *Astrophys. J.*, 780:111, 2014.
- [69] J. Kwan, K. Heitmann, S. Habib, N. Padmanabhan, H. Finkel, N. Frontiere, and A. Pope. 2013. e-Print: arXiv:1311.6444.
- [70] We do not consider models with spatial curvature in this article, and we note that the fluid approximation itself breaks down due to multi-streaming at small scales, limiting the reach of fluid-based perturbation theories.